ELSEVIER

Contents lists available at ScienceDirect

# Journal of Catalysis

journal homepage: www.elsevier.com/locate/jcat



### Research article

# Electrocatalytic hydrogenation of phenol on platinum-cobalt alloys

James Akinola<sup>1</sup>, Isaiah Barth<sup>1</sup>, Bryan R. Goldsmith<sup>\*</sup>, Nirala Singh<sup>\*</sup>

Department of Chemical Engineering, University of Michigan, Ann Arbor, MI 48109-2136, USA Catalysis Science and Technology Institute, University of Michigan, Ann Arbor, MI 48109-2136, USA



Keywords:
Bio-oil
Hydrogenation
Langmuir-Hinshelwood model
Hydrogen adsorption energy
Hydrogen evolution reaction



Here we investigate platinum-cobalt alloys to determine catalyst properties that control electrocatalytic hydrogenation (ECH) of phenol and the competing hydrogen evolution reaction (HER). We perform ECH of phenol on  $Pt_xCo_y$  nanoparticles and demonstrate that under certain potentials  $Pt_xCo_y$  alloys are more active than  $Pt_x$ . However, the ECH activity does not correlate directly with the hydrogen adsorption energy ( $\Delta G_H$ ), unlike what we find for HER. Combined electrochemical measurements, density functional theory (DFT) calculations, and kinetic modeling reveal that  $\Delta G_H$  is an insufficient descriptor for phenol ECH because the activation enthalpies for hydrogenation elementary steps scale more closely with their reaction enthalpies, which are more endothermic on  $Pt_xCo_y$  compared to  $Pt_x$ . Through DFT modeling we show the relationship between hydrogenation activation enthalpies and  $Co_x$  content depends strongly on whether the catalyst surface is a  $Pt_x$  skin or contains both  $Pt_x$  and  $Co_x$  alones. By incorporating the computed activation enthalpies into a kinetic model, we describe the qualitative trends in experimental ECH kinetics of phenol on  $Pt_xCo_y$  alloys as a function of applied potential and  $Co_x$  composition.

### 1. Introduction

The search for sustainable energy and chemicals has led to a growing interest in hydrogen-related processes, such as the hydrogen evolution reaction (HER) and electrocatalytic hydrogenation (ECH) of bio-oil. Electrocatalytic hydrogenation offers a sustainable pathway to stabilize lignin-derived bio-oil on the route to producing specialty chemicals and transportation fuels [1–7]. Understanding the mechanism and catalyst structure–activity relations for ECH of components of bio-oil may aid the transition to sustainable chemical and fuel production. In this study, we investigate phenol in aqueous acetate buffer as a representative lignin-derived phenolic compound in bio-oil [8], and we study ECH on Pt alloyed with Co ( $Pt_xCo_y$ ) to understand the mechanism and alloy nanoparticle catalyst design rules.

Electrocatalytic hydrogenation of phenol on Pt follows a Langmuir-Hinshelwood mechanism, such that the reaction rate is governed, in part, by the adsorption energies of hydrogen and phenol [9,10]. Surface-adsorbed hydrogen can either hydrogenate the phenol or combine via HER to form  $H_2$  as a side reaction. There are multiple examples of controlling the adsorption energies of reactants through alloying for thermocatalytic hydrogenation (TCH) [11-18]. Gas-phase TCH of

cyclohexene on Pt alloyed with Fe, Co, Ni, or Cu reached a maximum activity at moderate cyclohexene and hydrogen adsorption energies [19]. The catalytic activity of Ni<sub>x</sub>Fe<sub>y</sub> alloys for hydrogenation of C=C, C=O, and C=N bonds positively correlate with weakening hydrogen adsorption, and Ni<sub>2</sub>Fe sites had the weakest hydrogen adsorption energy and highest hydrogenation activity [20]. Hydrogen adsorption energy ( $\Delta G_H$ ) is also an effective descriptor for the HER activity of metals and alloys [21–27]. There are much fewer studies using alloys for ECH of organics [28–30], and the use of organic adsorption energy and  $\Delta G_H$  as ECH descriptors is underexplored. Generally, there is limited understanding of how alloying affects adsorption energies and reaction barriers of organics in the aqueous phase and whether  $\Delta G_H$  is a useful descriptor for ECH activity.

Whether a simple descriptor for ECH exists may depend on the structure of the alloy surface under reaction conditions. The activity of alloys is highly dependent on the composition of the surface and subsurface as well as nanostructure through strain [31–33], ligand [34,35], and ensemble effects [36,37]. The possibility of enrichment of certain elements in the catalyst surface is particularly important under reaction conditions where catalyst restructuring is possible and difficult to detect [38]. For example, Oezaslan  $\it et al.$  report that  $Pt_xCo_y$  forms a Pt skin in

E-mail addresses: bgoldsm@umich.edu (B.R. Goldsmith), snirala@umich.edu (N. Singh).

<sup>\*</sup> Corresponding authors.

these authors have contributed equally.

 $0.1 \text{ M HClO}_4$  [39], whereas others report that the surface in  $0.1 \text{ M HClO}_4$  or  $1 \text{ M HNO}_3$  consists of a mixture of Pt and Co atoms rather than a pure Pt skin [40–42]. The activity of a surface consisting only of Pt atoms may differ considerably from a catalyst surface consisting of both Pt and Co atoms in close proximity, even if the subsurface composition is similar.

In this work, we synthesize and characterize PtxCov alloys of different Co compositions to understand how the catalyst structure and hydrogen adsorption energy are related to ECH activity and current efficiency. We select these PtxCov alloys because Pt is an active metal for ECH and subsurface alloying of Co is reported to weaken the hydrogen adsorption energy as a result of compressive strain and ligand effects [31,33,34]. We postulate that weakening the hydrogen adsorption energy will enhance HER activity, but ECH activity will depend more strongly on the nanostructure and presence of surface Co in the Pt<sub>x</sub>Co<sub>y</sub>. Our X-ray absorption spectroscopy (XAS) and scanning transmission electron microscopy (STEM) characterization of the Pt<sub>x</sub>Co<sub>y</sub> alloy nanoparticles show that although the surface is enriched in Pt rather than Co relative to the bulk, the surfaces are still a mixture of Pt and Co atoms (as opposed to a pure Pt skin over a Pt<sub>x</sub>Co<sub>v</sub> core). On our Pt<sub>x</sub>Co<sub>v</sub> alloys, the ECH activity does not simply trend with the hydrogen adsorption energy. Our density functional theory (DFT) calculations indicate that the ECH activities of these alloys cannot be described by the  $\Delta G_{\rm H}$  alone because hydrogenation barriers tend to follow a Brønsted-Evans-Polanyi relationship with respect to the reaction energies of phenol hydrogenation, and surfaces with weaker hydrogen adsorption energies do not necessarily have lower hydrogenation barriers. We demonstrate how kinetic modeling is able to qualitatively describe the experimental activity of these alloys by incorporating not only the  $\Delta G_{\rm H}$  but also computed transition state energies on the mixed Pt and Co surfaces.

### 2. Experimental & computational methods

### 2.1. Chemicals and materials

All chemicals purchased were used as received. Chloroplatinic acid hexahydrate, H<sub>2</sub>PtCl<sub>6</sub>·6H<sub>2</sub>O (38-40 % Pt, Sigma Aldrich) and cobalt hydroxide, Co(OH)2 (95 %, Sigma Aldrich) were used as metal precursors for catalyst synthesis. 37 % HCl (Sigma Aldrich) was used to neutralize alkaline Co(OH)<sub>2</sub>. Sodium borohydride, NaBH<sub>4</sub> (≥96 %, Sigma Aldrich) was used as the chemical reductant. Carbon felt (6.35 mm thick, 99.0 %, Alfa Aesar) was used as the conductive porous support for ECH measurements. A graphite rod (3.05 mm diameter, 99.9995 %, Alfa Aesar) connected to carbon felt was used as the working electrode. Sodium acetate buffer solution (Sigma Aldrich, 3 M, pH 5.2) was used as supporting electrolyte for ECH and HER. Metal catalysts on Vulcan carbon, that is, 30 wt% Pt/C, 40 wt% Pt<sub>3</sub>Co/C, and 40 wt% PtCo/C were purchased from the Fuel Cell store. A 5 % Nafion 117 solution (Sigma Aldrich) was used as the binder for preparing catalyst inks for HER measurements. Boron nitride (99.5 %, Alfa Aesar) was used to pelletize the metal catalysts for ex-situ X-ray absorption spectroscopy measurements.

## 2.2. Catalyst preparation

Two sets of  $Pt_xCo_y$  alloys were prepared.  $Pt_xCo_y/C$  refers to purchased nanoparticles of  $Pt_xCo_y$  supported on Vulcan carbon.  $Pt_xCo_y/C$  were used to measure HER activity on a rotating disk electrode (RDE).  $Pt_xCo_y/f$ elt denotes  $Pt_xCo_y$  nanoparticles synthesized on a conductive porous carbon felt.  $Pt_xCo_y/f$ elt were used for ECH activity measurements because higher surface area catalysts were needed for product quantification and because of difficulties in loading the  $Pt_xCo_y/C$  onto a porous support without mechanical loss of catalyst at the negative potentials explored in this work. Both sets of samples were electrochemically cycled prior to testing for activity to avoid any leaching during activity measurements. This pretreatment process is described below.

Preparation of platinum-cobalt alloy nanoparticles on Vulcan carbon for

rotating disk electrode. To perform HER measurements using a RDE, catalysts inks were prepared by adding 3 mg of the supported catalyst (i. e., 30 wt% Pt/C, 40 wt% Pt<sub>3</sub>Co/C, or 40 wt% PtCo/C) into a mixture of 2.5 mL Millipore water and 2.5 mL isopropyl alcohol and 17.5  $\mu$ L of 5 wt % Nafion solution as the binding agent. The mixture was sonicated for 2 hr to disperse the catalyst in the solution. A glassy carbon disk substrate for the inks was thoroughly polished using a 0.05  $\mu$ m alumina suspension and rinsed three times with Millipore water and then sonicated in water for 30 min. 8  $\mu$ L of the freshly sonicated catalyst ink was deposited on the clean glassy carbon disk substrate assembled in a Teflon rotating disk holder in two separate depositions (16  $\mu$ L total) performed 30 min apart to achieve a catalyst loading of 9.6  $\mu$ g. The deposited catalysts were air dried in a closed compartment for at least 1 hr to form a catalyst film before experiments.

Synthesis of platinum-cobalt alloy nanoparticles on porous carbon felt *support.* Pieces of carbon felt (1.5 cm  $\times$  1.5 cm  $\times$  6.35 mm thick) were first thermally pretreated in air at 400 °C for 16 hr to increase their surface area. Pt<sub>x</sub>Co<sub>y</sub> was directly synthesized on carbon felts by chemical reduction using a sodium borohydride method [43]. The target compositions of Pt and Co were adjusted to synthesize Pt/felt, Pt<sub>3</sub>Co/felt, PtCo/felt, and PtCo<sub>3</sub>/felt. An amount of Co(OH)<sub>2</sub> to achieve the desired Co metal loading and metal atomic ratio was dissolved in 20 mL mixture of 1:1 vol ratio of methanol to Millipore water. After, 37 % HCl was added dropwise with a precision pipette to bring the solution to pH 2. Similarly, the desired amount of H2PtCl6·6H2O was used to prepare a separate 20 mL aqueous solution of chloroplatinic acid. The two solutions were mixed, and the wetted carbon felt was sonicated in the solution for 2 hr. NaBH<sub>4</sub> was added to 5 mL of water in a separate vial to achieve NaBH4:metal molar ratio of 12:1. Sodium borohydride solution was added dropwise to the precursor solution containing the felt in a water bath and sonicated for 3 hr. The felt was afterwards removed from the solution, rinsed three times with Millipore water, and left to dry in a vacuum oven set at 80 °C for 15 hr. Before use for ECH measurements, the felt was thoroughly rinsed with Millipore water.

### 2.3. Catalyst characterization and surface area measurements

Pretreatment of platinum-cobalt alloys before use. To minimize dissolution of Co during activity testing, the  $Pt_xCo_y$  catalysts were first subjected to cyclic voltammetry by applying 1500 potential sweeps between 0.05 and 1.5 V vs. RHE at 500 mV s $^{-1}$  in acetate buffer. The same procedure was used for the  $Pt_xCo_y/C$  and  $Pt_xCo_y/f$ elt samples and is based on a protocol that is known to both remove any residual unalloyed Co in the catalyst and leach Co from the  $Pt_xCo_y/C$  surface. This process is reported to result in either a Pt shell with a  $Pt_xCo_y$  core or to form an enriched Pt surface although with surface Co present (i.e., a mixed alloy surface) [40–42]. Our results here indicate that we form a mixed alloy surface that contains both Pt and Co as described in the Results and Discussion. The pretreated catalysts following cyclic voltammetry were used for all HER and ECH activity measurements and all characterization except where specified otherwise.

Bulk elemental analysis. The Pt and Co loadings of the as prepared  $Pt_xCo_y$  and pretreated  $Pt_xCo_y$  catalysts (i.e., following cyclic voltammetry) were measured using a PerkinElmer NexION 2000 ICP-MS. 1 mg of the catalyst was digested in 2 mL aqua regia solution (3:1 M HCl: HNO\_3). This solution was further diluted with Millipore water by a factor of 10,000 to about 10–20 ppb. 20 ppb bismuth and 20 ppb scandium were co-fed as internal standard in the instrument to normalize Pt and Co intensities, respectively. The concentrations of Pt and Co were extracted by comparing to calibration standards of Pt and Co. The composition of the pretreated catalysts based on inductively coupled plasma-mass spectrometry (ICP-MS) is used for the catalyst naming convention.

*X-ray absorption spectroscopy.* The pretreated  $Pt_xCo_y/C$  and  $Pt_xCo_y/C$  felt catalysts were crushed to powder and mixed with calculated amounts of boron nitride as a pelletizer to obtain desired edge steps and

X-ray transmission through the samples. The catalysts and boron nitride were made into pellets (13 mm diameter and 1-2 mm thick) and probed at the Pt L3-edge (11564 eV) and Co K-edge (7709 eV). These samples were also analyzed in our custom made in-situ XAS cell [44] under negative cathodic potential with and without phenol in the supporting electrolyte to understand the catalyst structure during ECH. Samples were analyzed in transmission mode or fluorescence mode depending on the quality of the data. In-situ XAS measurements were performed only in fluorescence mode because of hydrogen bubble formation that interfered with transmission signal. A minimum of three scans were taken for each sample at either edge. Pre-processing and linear combination fitting of the X-ray absorption near edge (XANES) region was performed using Athena while extended X-ray absorption fine structure (EXAFS) fitting was performed using Artemis [45]. Pt and Co foils were used as standards for either edge and used as reference in data alignment and fitting.

X-ray diffraction (XRD). X-ray diffraction was performed on the  $Pt_xCo_y/C$  and  $Pt_xCo_y/felt$  catalysts using a Rigaku Miniflex X-ray diffractometer with Cu Kα radiation and a Ni filter that has an X-ray wavelength of 1.5406 Å. For the  $Pt_xCo_y/felt$  samples, 10 mg of the catalyst on felt was crushed to powder and put into a transparent sample holder before setting the voltage and current to 40 kV and 15 mA, respectively. For the  $Pt_xCo_y/C$  samples, the powder was directly used. Scanning was carried out at  $3^\circ/min$  with a  $0.02^\circ$  step in the range of  $10^\circ < 2\theta < 90^\circ$ . The Scherrer equation was used to estimate the average crystallite size as discussed in the SI.

Transmission electron microscopy (TEM) and scanning transmission electron microscopy (STEM) measurements. A Thermo Fisher Scientific Talos F200X G2 electron microscope equipped with a Super-X EDX detector and operating at an accelerating voltage of 200 keV was used for the STEM and TEM imaging and analysis. High-angle annular dark-field scanning transmission electron microscopy (HAADF-STEM) was used to obtain surface imaging because of its high image resolution [46,47]. In addition, energy-dispersive X-ray spectroscopy (EDS) element mapping and line scans were used to determine variations in the metal composition along the diameter of a single nanoparticle. A portion of the catalyst on carbon felt was ground before dissolving 1 mg of the ground catalyst in 1 mL of isopropanol. A drop of the suspension was deposited on a clean Cu grid. The Cu grid was left to dry overnight before imaging was performed. The average size and distribution of particles were acquired with the ImageJ software.

Hydrogen underpotential deposition ( $H_{UPD}$ ). The electrochemically active surface area (ECSA) of exposed Pt surface metal atoms on the  $Pt_xCo_y/felt$  and  $Pt_xCo_y/C$  catalysts was measured using  $H_{UPD}$ . The catalysts were electrochemically cleaned using cyclic voltammetry (CV) at 100 mV s<sup>-1</sup> for 50 cycles at potentials -0.2 to 1.5 V vs. RHE. After electrochemical cleaning, CV was done at a 20 mV s<sup>-1</sup> scan rate in the potential window of 0.05 V to 1.2 V and the  $H_{UPD}$  charge from the oxidative region after subtracting the baseline capacitive charge was used to estimate the ECSA of the Pt sites using a charge density of 210  $\mu$ C cm<sup>-2</sup>.

## 2.4. Hydrogen evolution reaction (HER)

Hydrogen evolution was performed in a 3 M acetate buffer solution in a three-electrode single compartment batch electrolysis cell at room temperature. The working electrode was a glassy carbon disk with the deposited catalysts assembly used in an RDE setup (Pine Instruments). A Ag/AgCl double junction electrode was used as the reference electrode and a Pt wire loop was used as the counter electrode. The catalysts were first pretreated as discussed above, and the ECSA was measured by  $\rm H_{UPD}$  before performing linear scan voltammetry at 10 mV s $^{-1}$  between -0.2 V and 1.1 V vs. RHE at rotation rates of 400, 900, 1600, and 2500 rpm. The applied potential was corrected for potential loss due to series resistance as measured by the real part of the impedance measured at high frequency. The measured current was normalized to ECSA to obtain

the current density. Based on the measurements, 1600 rpm was sufficiently high that mass transport artifacts were not observed (Figure S1a-c), thus the current densities at 1600 rpm were used to evaluate intrinsic kinetics (kinetic current density). Tafel plots were constructed by plotting the log of the current density at 1600 rpm against the overvoltage for the HER rates (Figure S1d). The Tafel slope and exchange current density were determined by fitting the log of current density vs. overvoltage to a linear line (log  $i=\eta/b+\log i_0$ ), where i is the kinetic current density, b is the Tafel slope,  $\eta$  is the overvoltage, and  $i_0$  is the exchange current density. Only overvoltage values  $\geq$  100 mV were used in the fit to the Tafel equation to extract the exchange current density.

### 2.5. Electrocatalytic hydrogenation of phenol

ECH measurement. ECH was performed on the PtxCov/felt catalysts using a two-compartment batch electrolysis cell where the cathodic and anodic compartments were separated with a Nafion 117 membrane. The Pt<sub>x</sub>Co<sub>v</sub>/felt catalysts were attached to a 3 mm diameter graphite rod (Sigma Aldrich, 99.99 %) and used as the working electrode in the 140 mL cathodic compartment. Acetate buffer (3 M, pH 5.2) sparged with N<sub>2</sub> was used as the supporting electrolyte in both cathodic and anodic compartments. A Ag/AgCl double junction electrode was used as the reference electrode and the counter electrode was a 3 mm diameter graphite rod (Sigma Aldrich, 99.99 %). To perform ECH, the target negative potential was first applied for 1 hr to the working electrode to reduce the metal nanoparticles and saturate the solution with hydrogen. Phenol sparged with N2 was added to the cathodic compartment to achieve 20 mM phenol concentration before performing ECH at a fixed potential of either -0.1, -0.15, or -0.2 V vs. RHE using a Bio-Logic VSP-300. The series resistance was automatically compensated at 85 % using impedance spectroscopy at a frequency of 200 kHz and the remaining 15% was manually corrected to give  $\pm 10$  mV of the reported iR-free applied potentials. The current densities during ECH under these constant cathodic potentials for the different PtxCov/felt catalysts are shown in Figure S2. No change in the pH of acetate buffer plus phenol solution before and after performing ECH for 2 hr was observed, indicating sufficient buffering capacity.

Product quantification during ECH of phenol. A 1 mL aliquot was taken from the cathodic compartment every 30 min to monitor ECH reaction progress. ECH products (i.e., cyclohexanone and cyclohexanol) and the phenol reactant were extracted from the aqueous supporting electrolyte into an organic phase using three sequential liquid-liquid extractions with ethyl acetate as the solvent. For every extraction step, about 5 mg of sodium chloride was added to the aliquot before mixing with 1 mL of pure ethyl acetate to aid separation of the organic and aqueous phase. Any water present in the organic phase was removed using anhydrous Na<sub>2</sub>SO<sub>4</sub> (Sigma Aldrich 99 %). Dimethoxybenzene (DMB) was used as an external standard, where 10 µL DMB was mixed with 1 mL of the dried organic phase before injecting 1 µL of the mixture to an Agilent Varian 450 gas chromatograph equipped with a flame ionization detector. ECH was performed at less than 10 % conversion and carbon balances were greater than 90 %. We report the measured cyclohexanol and cyclohexanone concentrations under differential conversion conditions at different applied potentials for the  $Pt_xCo_y/felt$  catalysts in Table S1. The turnover frequency (TOF) for each PtxCoy/felt catalyst was calculated from the rate of cyclohexanol and cyclohexanone formed per surface Pt atom estimated from the hydrogen underpotential deposition.

### 2.6. Density functional theory modeling

The Vienna Ab initio Simulation Package (VASP) was used for Kohn-Sham DFT calculations [48–51]. The exchange–correlation energy was calculated using the Perdew-Burke-Ernzerhof functional [52] with the semi-empirical D3 dispersion correction [53]. The projector augmented wave method and a plane wave kinetic energy cutoff of 400 eV were

used for all calculations [54,55]. The first-order Methfessel-Paxton smearing scheme with a 0.2 eV smearing width was used [56]. All calculations performed on slabs containing Co were spin-polarized. Spin polarization had a negligible effect on the pure Pt surface.

We modeled Pt and PtxCov intermetallics (i.e., Pt, Pt3Co, PtCo, and PtCo<sub>3</sub>) and Pt/Pt<sub>x</sub>Co<sub>y</sub> (i.e., a monolayer of pure Pt over a Pt<sub>x</sub>Co<sub>y</sub> subsurface) systems to investigate how Pt enrichment in the alloy surface affects adsorption of phenol and hydrogen and the catalytic performance for HER and ECH. Four-atom bulk face-centered cubic (FCC) unit cells of Pt, Pt<sub>3</sub>Co, PtCo, and PtCo<sub>3</sub> were optimized in VASP with a 21  $\times$  21  $\times$  21 Monkhorst-Pack k-point grid [57]. We modeled only the FCC crystal structure because it is the crystal structure observed experimentally in our purchased and synthesized catalysts from XRD. The expected change in lattice constant with Co fraction (i.e., from Vegard's law) from the FCC lattice constants matches the change in lattice constant from our powder XRD data for PtxCov/C for their expected Co fraction (Figure S3), indicating alloys are formed. Previous work found that the (111) facet of Pt and other metals like Rh are the active facet for hydrogenation of aromatics [58,59]. Therefore, we constructed the (111) facets of Pt, Pt<sub>3</sub>Co, PtCo, and PtCo<sub>3</sub> from the bulk unit cells. The Pt/ Pt<sub>v</sub>Co<sub>v</sub> slabs were modeled by replacing all Co atoms in the top layer of the slabs with Pt to achieve a pure Pt surface layer. The Pt<sub>v</sub>Co<sub>v</sub> and Pt/

 $Pt_vCo_v$  systems were modeled using  $4 \times 4 \times 4$  slabs, where the bottom two layers were fixed in their bulk lattice coordinates and the top two layers were relaxed during geometry optimization. A 3 imes 3 imes 1 Mokhorst-Pack k-point grid was used for all slab calculations. The climbing-image nudged elastic band method was used to find the transition states for the hydrogenation reactions [60]. The enthalpies and free energies of adsorbed phenol, hydrogen, and reaction intermediates were evaluated in the harmonic limit without solvation corrections, and the free energies of non-adsorbed species were evaluated using ideal gas thermodynamic corrections at 300 K. The configurations of phenol and hydrogen with the lowest computed energies were used in the subsequent work. Implicit solvation was not used to model adsorption or hydrogenation because it was found to improperly describe solvent effects for phenol adsorption and had little effect on the adsorption energies of hydrogen or the hydrogenation barriers using default parameters [58,61]. All optimized geometries of surfaces and adsorbate/surface structures are available in the supplemental information.

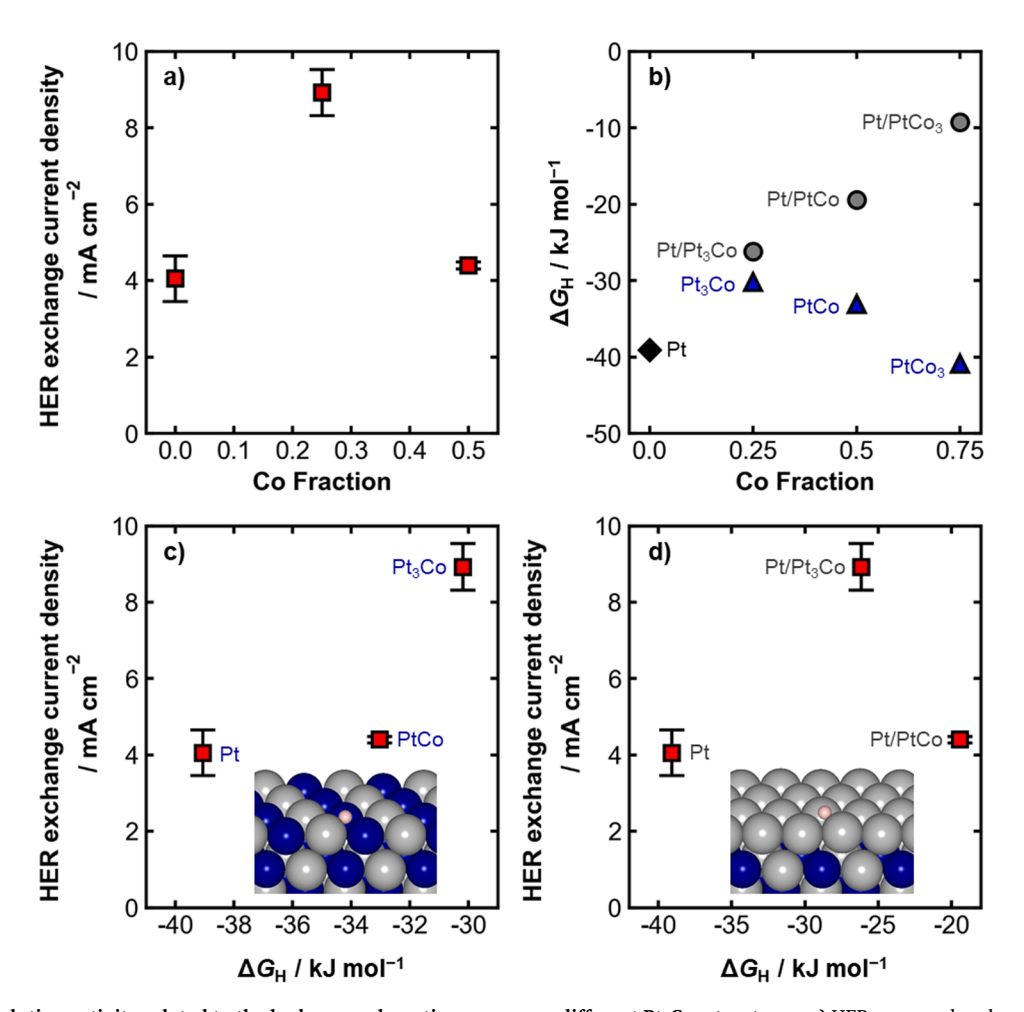


Fig. 1. Hydrogen evolution activity related to the hydrogen adsorption energy on different  $Pt_xCo_y$  structures. a) HER measured exchange current densities at 23.3 °C as a function of Co fraction for the  $Pt_xCo_y$ /C catalysts. Exchange current densities were extracted from Tafel plots shown in the supplemental information for the  $Pt_xCo_y$ /C catalysts deposited on glassy carbon in 3 M acetate buffer supporting electrolyte (pH 5.2) sparged with  $H_2$ . b) DFT-calculated hydrogen adsorption free energies on  $Pt_xCo_y$  alloys as a function of Co content at 300 K. c) Measured HER exchange current densities as a function of the calculated hydrogen adsorption free energies on  $Pt_xCo_y$  alloys. d) HER measured exchange current densities as a function of the calculated hydrogen adsorption free energies on  $Pt_xCo_y$  alloys. Images of hydrogen adsorbed on PtCo and Pt/PtCo alloy slabs are inset in c) and d), respectively. Hydrogen is colored peach, Pt is colored gray, and Co is colored blue. Error bars for a), c) and d) denote the standard deviation from the average of two separate experiments. (For interpretation of the references to color in this figure legend, the reader is referred to the web version of this article.)

### 3. Results and discussion

# 3.1. Comparing hydrogen evolution activity to hydrogen adsorption energy on $Pt_xCo_y/C$

In Fig. 1a we show the HER exchange current densities on  $Pt_xCo_y/C$  catalysts as a function of Co fraction.  $Pt_3Co/C$  is the most active for HER, followed by PtCo/C and Pt/C. The exchange current density of Pt/C in acetate buffer (pH 5.2) obtained here (4.1 mA cm $^{-2}$ ) matches that reported by Zheng and coworkers (4.0 mA cm $^{-2}$ ) in the same electrolyte and pH [22]. The HER activity trend between Pt/C and  $Pt_3Co/C$  is consistent with studies that reported  $Pt_3Co$  to be superior to  $Pt_3Co/C$  is although the structure of the  $Pt_3Co$  surface impacts the HER performance. Specifically, a  $Pt_3Co$  catalyst with both Pt and Co present on the surface and a  $Pt_3Co$  catalyst with a pure Pt surface layer were reported to increase the current density by two and five times compared to pure Pt, respectively [42].

Exposing  $Pt_xCo_y$  catalysts to acidic conditions can form a Pt-enriched surface (i.e., a surface with both Pt and Co) or a Pt-skin structure on a  $Pt_xCo_y$  core. However, the structure of  $Pt_xCo_y$  alloys in our supporting electrolyte (3 M acetate buffer, pH 5) has never been reported. The enhancement we observe in Fig. 1a for  $Pt_3Co/C$  compared to Pt/C (a factor of 2.25) is close to the reported enhancement for a  $Pt_3Co$  catalyst with both Pt and Co present on the surface. Although there are reports of sub-nanometer PtCo clusters with enhanced HER activity relative to pure Pt [63], our PtCo/C, with a diameter of approximately 5 nm (characterization provided below), is less active than  $Pt_3Co/C$  and more similar to Pt/C.

To better understand the trends in HER exchange current densities on the Pt<sub>x</sub>Co<sub>v</sub>/C catalysts, we use DFT to model hydrogen adsorption on Pt<sub>x</sub>Co<sub>v</sub> for two possible types of structures: 1) both Pt and Co present in the surface and 2) a pure Pt surface covering a  $Pt_xCo_y$  core  $(Pt/Pt_xCo_y)$ . Here we consider the alloys to form either a mixed Pt<sub>x</sub>Co<sub>y</sub> surface or a Pt surface covering a PtxCov core, but it is possible that the surface structure of the alloys depends on the total Co content. Although the results in Fig. 1 cannot rule out this possibility, our computed segregation energies and other characterizations discussed in the following section suggest that the mixed PtxCov surface is favorable for all Co contents studied here under applied potential. In Fig. 1b we show that an increasing Co fraction in Pt/PtxCov alloys causes the surface Pt to adsorb H weaker, but high fractions of Co in the surface of PtxCov alloys cause the surface to behave more like Co and bind H more strongly ( $\Delta G_{\rm H}$  on Co(0001) is computed to be  $-42 \text{ kJ mol}^{-1}$ ). For Pt/Pt<sub>x</sub>Co<sub>y</sub> the presence of Co in the alloy subsurface interacts with the Pt overlayer through a combination of strain and ligand effects [64-66] to cause a monotonic weakening of the computed hydrogen adsorption energy as Co increases. For the mixed PtxCov surfaces, the hydrogen adsorption energy weakens initially in the Pt<sub>3</sub>Co case but then strengthens with increasing Co in the PtCo and PtCo3 cases because of the strong Co-H interactions that are possible when high fractions of Co are on the surface. In fact, the threefold Co sites on PtCo3 are predicted to adsorb hydrogen only ~1 kJ mol<sup>-1</sup> weaker than a pure Co(0001) surface.

By comparing the experimental HER exchange current density to the computed  $\Delta G_{\rm H}$ , we hypothesize that our experimental catalysts form a mixed Pt and Co surface rather than a Pt skin on a Pt<sub>x</sub>Co<sub>y</sub> core. We show the experimental HER exchange current density for the Pt<sub>x</sub>Co<sub>y</sub>/C catalysts against the computed  $\Delta G_{\rm H}$  assuming a mixture of Pt and Co on the surface in Fig. 1c. We do the same for a Pt/Pt<sub>x</sub>Co<sub>y</sub> structure in Fig. 1d. For the mixed Co and Pt surface, the HER exchange current density increases with weakening hydrogen adsorption (Fig. 1c). The HER exchange current density does not increase with weakening of the predicted hydrogen adsorption on the Pt/Pt<sub>x</sub>Co<sub>y</sub> models (Fig. 1d). Because generally HER activity for Pt group metals is expected to increase with weakening hydrogen adsorption in acids [22,27], the results in Fig. 1c compared to Fig. 1d indicate that the Pt<sub>x</sub>Co<sub>y</sub>/C catalysts pretreated in 3 M acetate buffer (pH 5.2) do not form a Pt skin, but instead

have both Pt and Co present on the catalyst surface. Although  $\rm H_2O^*$  and OH\* adsorption energies are proposed to be descriptors for HER in alkaline media [67,68], we focus on  $\Delta G_{\rm H}$  because H\* is more relevant for phenol ECH in acetate buffer (pH 5). We include the adsorption energies of water on the different surfaces and plot them against the HER exchange current densities in Figure S4. Like  $\Delta G_{\rm H}$ , there is a correlation between the HER activity and water adsorption energy on the mixed surfaces, but not on the Pt/PtxCov surfaces.

Using DFT, we calculate the energy to substitute subsurface Co with surface Pt in a Pt/PtxCov slab with and without adsorbed hydrogen to predict the preferred structure of the slabs. Our calculations suggest that the presence of H\*, which interacts more strongly with Co than with Pt, has the potential to stabilize Co in the catalyst surface at high H\* coverages (Figure S5). The thermodynamic stability of Co in the alloy surface compared to the alloy subsurface depends on factors such as the Co fraction in the alloy and the coverage of hydrogen on the surface. A pure Pt surface is thermodynamically favorable at all Co fractions for bare surfaces. At high hydrogen coverages (i.e., 1 ML), a mixed Pt<sub>x</sub>Co<sub>y</sub> surface is predicted to be thermodynamically favorable for the Pt<sub>3</sub>Co, PtCo, and PtCo<sub>3</sub> systems. At 0.25 ML H\* coverage, however, a Pt/Pt<sub>v</sub>Co<sub>v</sub> structure is thermodynamically preferred for alloys with lower Co fractions (Pt<sub>3</sub>Co and PtCo in Figure \$5b). Our microkinetic modeling predictions for phenol ECH (discussed in section 3.5) predict that H\* coverage is typically higher than 0.25 ML H\* for Pt<sub>3</sub>Co at the potentials we study experimentally. This modeling prediction corroborates our observation of the HER enhancement of Pt<sub>3</sub>Co/C compared to Pt/C matching what is expected for a surface with both Pt and Co present. The dependence of  $\Delta G_{\rm H}$  on the Pt<sub>x</sub>Co<sub>v</sub> structure highlights the importance of identifying the surface composition for electrocatalysis, because a Pt/ PtxCov catalyst may have considerably different activity than a PtxCov catalyst.

# 3.2. Synthesis and characterization of $Pt_xCo_y$ alloys supported on conductive carbon felt

To measure ECH activity for  $Pt_xCo_y$  alloys, we synthesize  $Pt_xCo_y$  nanoparticles with varying compositions of Co directly on a conductive carbon felt support ( $Pt_xCo_y$ /felt) to achieve sufficiently high catalyst loading to detect the products of ECH of phenol (cyclohexanol and cyclohexanone). We cycle these catalysts from 0.05-1.5~V vs. RHE prior to use for ECH and do not detect any remaining unalloyed Co (Figures S6, S7, S8), implying alloys are formed rather than mixtures of bulk Co and Pt [41]. Although these catalysts are synthesized by chemical reduction on carbon felt support as opposed to the catalysts shown in Fig. 1 ( $Pt_xCo_y/C$ , supported on Vulcan carbon), we show below that they form similar structures.

We show Pt  $L_3$ -edge EXAFS of the  $Pt_xCo_y$ /felt samples in Fig. 2a that confirms local coordination of Co with Pt. The Pt-Pt bond length of the  $Pt_{100}$ /felt matches that of a Pt foil. This Pt-Pt bond length decreases with increasing bulk Co content as measured by ICP-MS. The peak between 2.4–2.6 Å indicates scattering between two nearest neighbor Pt atoms in the first shell. Pt atoms are replaced by smaller Co atoms with increasing Co content, which leads to smaller interatomic distances. The fits of the EXAFS data of the Pt foil and the  $Pt_xCo_y$ /felt are shown in Figures S9, S10, S11 and the Pt-Pt and Pt-Co coordination number and bond lengths extracted from the fits to a first and second shell are shown in Table S2. With increasing Co content, we also see an increase in the Pt-Co coordination numbers, further indicating the formation of alloys.

Our measured lattice constant of the alloys from XRD also corroborates the formation of  $Pt_xCo_y$  alloys. We show the XRD patterns for the  $Pt_xCo_y$ /felt catalysts in Fig. 2b with the Pt FCC lattice peak highlighted. There is no evidence of pure Co phases in the XRD. The Pt FCC peak shifts to higher 2 $\theta$  values compared to Pt, shown in the inset image in Fig. 2b. We calculate the Co fraction from the shift of the 2 $\theta$  values of the (1 1 1) plane using Vegard's law (Figure S3) and plot this Co fraction from XRD in Fig. 2c along with the fraction of Co in the lattice based on

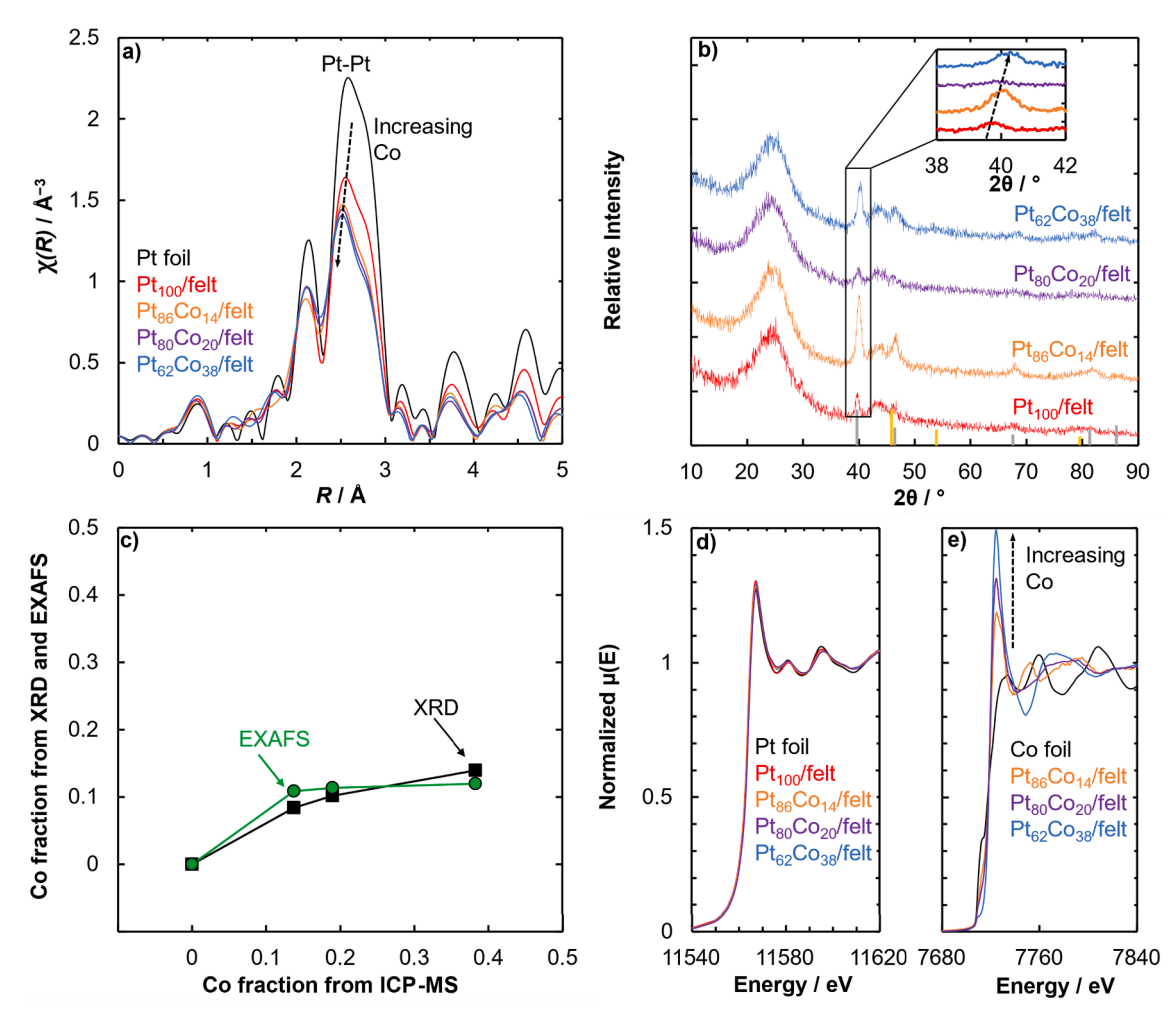


Fig. 2. Ex-situ XAS and XRD for  $Pt_xCo_y$ /felt catalysts. a) Unadjusted k-weighted EXAFS spectra of Pt foil and  $Pt_xCo_y$ /felt in real space collected at the Pt  $L_3$ -edge. b) XRD spectra of  $Pt_xCo_y$ /felt with Pt #04–0802 and Co #15–0806 standards indicated by ash and gold vertical lines, respectively. Inset corresponds to region attributed to (111). c) Co fraction from XRD and EXAFS as a function of the Co fraction measured from ICP-MS. The x and y in  $Pt_xCo_y$  are the bulk atomic ratio of Pt and Co measured from ICP-MS after pretreatment. Normalized XANES spectra of metal foils and  $Pt_xCo_y$ /felt catalysts at the d) Pt  $L_3$ -edge and e) Co K-edge.

the fitted EXAFS data using the Pt-Pt and Pt-Co coordination numbers. The Co fraction from EXAFS and XRD are similar to one another, but they differ quantitatively from the Co fraction measured using ICP-MS, although they follow the same qualitative trend. Although the higher Co content measured from ICP-MS following complete dissolution of the catalyst may indicate some unalloyed Co in the catalyst, we do not see any indication of pure Co or Co oxide redox reactions based on the cyclic voltammetry following our pretreatment (Figure S7). One possibility is that excess cobalt may arise from unalloyed Co in the catalyst core that is not in contact with the electrolyte. Thus, this excess bulk Co should not influence the surface reaction.

The  $Pt_xCo_y$ /felt catalysts are only slightly oxidized ex-situ and mostly metallic under applied cathodic potential. We show in Fig. 2d and Fig. 2e the ex-situ XANES of the catalysts on felt at the Pt L<sub>3</sub>-edge and Co K-edge. The shape and intensity of the white line for the metallic Pt foil is similar to that of the  $Pt_xCo_y$ /felt samples, indicating Pt is mainly in the metallic phase. Using linear combination analysis of the XANES data in Fig. 2d compared to Pt foil and PtO<sub>2</sub> (Table S3) we show that less than 2 % of Pt forms PtO<sub>2</sub>. We expect 20 % of all bulk Pt to be on the surface based on an average particle size of 5 nm, thus only a small fraction of the surface Pt seems to be oxidized. Under applied cathodic potential (-0.05 V vs. RHE), the XANES of Pt<sub>100</sub>/felt in Figure S12 show a white line similar to that of the metallic Pt foil except for the broad shoulder indicating the formation of adsorbed H on Pt at negative potentials [44]. Thus, we do not expect significant differences in the electronic structure

of Pt during operating conditions. Contrary to the Pt  $L_3$ -edge, the white line at the Co K-edge in Fig. 2e increases with Co content which could indicate the formation of oxidized Co species. These oxidized Co species are likely from surface Co because subsurface Co would not be exposed to air. This observation of surface oxidized Co is similar to reports of surface oxidized Ni in PtNi alloys, which was interpreted as being due to Ni in the surface [69,70]. The presence of oxidized surface Co suggests that  $Pt_xCo_y$  do not form a Pt skin, but rather there is Co present on the surface. In alkaline conditions (pH 13), oxidized Co can form stable nanoislands of  $Co(OH)_2$  randomly distributed over Pt [71]. We were unable to evaluate the Co K-edge under operating conditions because of the noise in the XANES signal from  $H_2$  bubble formation, but we hypothesize Co may reduce under the potentials relevant for ECH performed in this work at pH 5.

The  $Pt_xCo_y$ /felt nanoparticles have similar particle sizes despite the variation in bulk Co fraction, so that differences in their ECH performance can be attributed to varying the Co content, rather than structure sensitivity effects [58,59]. We have previously shown that phenol ECH on Pt and Rh is a structure sensitive reaction [58], with larger particles with a higher fraction of terrace sites showing higher turnover frequencies. The TEM images and distribution in Fig. 3a, 3b, and 3d show that  $Pt_{100}$ /felt,  $Pt_{86}Co_{14}$ /felt and  $Pt_{80}Co_{20}$ /felt have similar average nanoparticle sizes (5.8  $\pm$  1.3 nm, 5.8  $\pm$  1.8 nm and 5.5  $\pm$  1.2 nm, respectively) and are well dispersed on the treated carbon felt (additional images are shown in Figure S13). Although the average particle

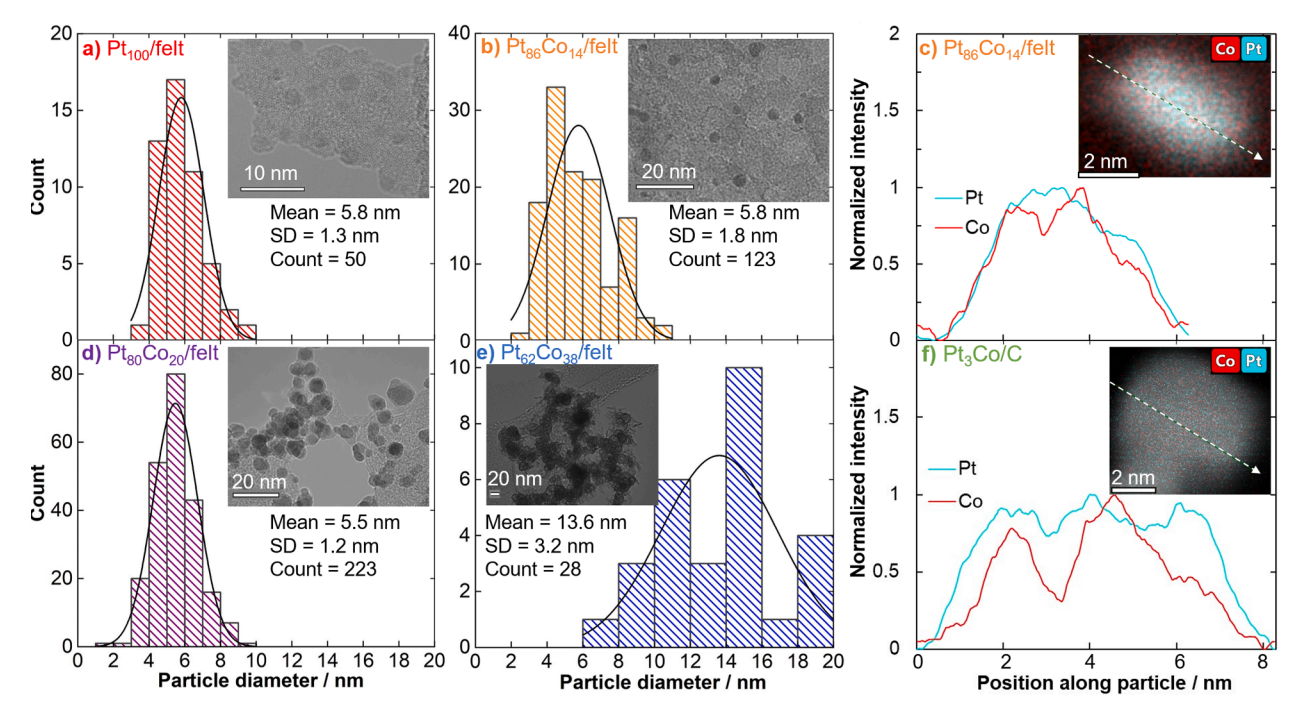


Fig. 3. TEM histogram distribution of particle diameters and HAADF-STEM imaging of  $Pt_xCo_y$  catalysts. Nanoparticle histogram distribution for a)  $Pt_{100}$ /felt, b)  $Pt_{86}Co_{14}$ /felt, d)  $Pt_{80}Co_{20}$ /felt, and e)  $Pt_{62}Co_{38}$ /felt. Inset images in a), b), d) and e) are representative micrographs of the catalysts. HAADF-STEM images and EDS line profile analysis across a single nanoparticle of the catalysts for c)  $Pt_{86}Co_{14}$ /felt, and f)  $Pt_{3}Co$ /C. Inset images in c) and f) shows a 2D elemental mapping of Pt (teal) and Co (red) across the nanoparticle for which the line scan was performed. (For interpretation of the references to color in this figure legend, the reader is referred to the web version of this article.)

size and distribution is larger for the  $Pt_{62}Co_{38}/\text{felt}$  catalyst in Fig. 3e (13.6  $\pm$  3.2 nm), the expected increase in activity because of a higher fraction of the active terraces was not observed as we will discuss in the subsequent section. We give the average nanoparticle sizes from TEM, XRD crystallite sizes calculated from the Scherrer equation, and the EXAFS first shell total coordination number in Table S4. The trend in particle sizes from these different methods in Table S4 are qualitatively in agreement.

We show by STEM-EDS line profile analysis for  $Pt_{86}Co_{14}/felt$  in Fig. 3c and  $Pt_{3}Co/C$  in Fig. 3f that both the carbon felt and Vulcan carbon supported catalysts do not form a Pt skin but instead form a surface with both Pt and Co present. The Co and Pt line scan across a

single nanoparticle shows a similar ratio of the Pt and Co intensity at the edges of the particles as in the core of the particle, indicating no visible Pt shell is formed. This technique has been used to identify core–shell particles in the literature [46,47]. HAADF-STEM imaging and EDS line scan analysis (Figure S14) for PtCo/C shows the surface also contains both Pt and Co. This further corroborates our evidence that both the  $Pt_xCo_y$  supported on carbon felt ( $Pt_xCo_y$ /felt) and  $Pt_xCo_y$  supported on Vulcan carbon ( $Pt_xCo_y$ /C) have a surface containing both Pt and Co atoms.

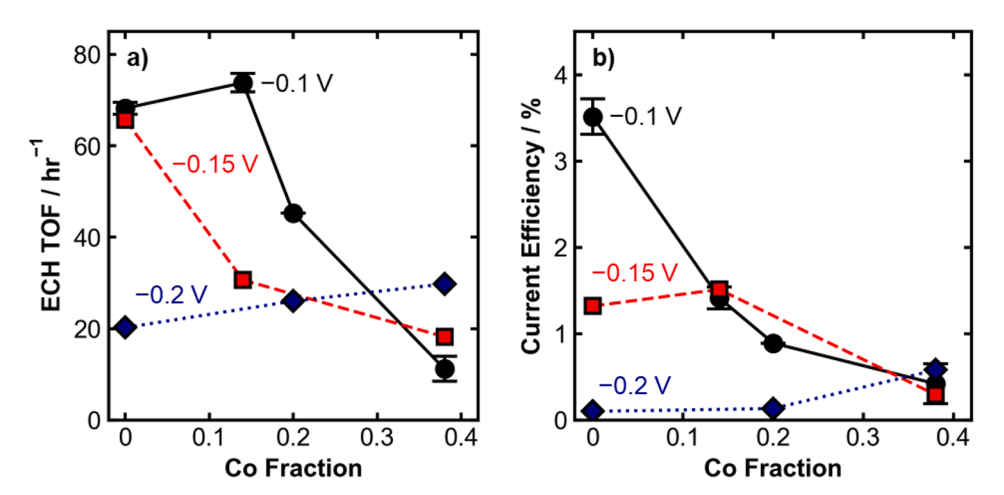


Fig. 4. Experimental ECH turnover frequency and current efficiency on  $Pt_xCo_y$ /felt catalysts as a function of Co fraction for different applied potentials. a) ECH TOF in 20 mM phenol in 3 M acetate buffer supporting electrolyte (pH 5.2) at 23.3 °C and -0.1, -0.15 or -0.2 V vs. RHE. The applied potential was directly corrected for 85 % of the series resistances using the potentiostat ZIR technique and the remaining 15 % series resistance was further corrected manually to give  $\pm 0.01$  V of target potential. The number of surface atoms of the catalysts used to calculate the TOF was estimated from the Pt  $H_{UPD}$  surface area. b) Current efficiency to ECH calculated from the moles of ECH products with respect to the amount of charge passed.

### 3.3. Electrocatalytic hydrogenation of phenol on Pt<sub>x</sub>Co<sub>y</sub> alloys

Unlike our observation that the hydrogen adsorption energy shows a clear trend with the HER activity (Fig. 1), the more complex ECH performance in Fig. 4 prevents us from using a simple descriptor to understand the PtxCov/felt catalysts. For example, the catalyst with the highest TOF at −0.1 V vs. RHE (Pt<sub>86</sub>Co<sub>14</sub>/felt) is not the most active at more negative potentials. The more negative potentials may result in lower ECH TOFs on the Pt100/felt and Pt86Co14/felt due to increased hydrogen coverage that blocks adsorption of phenol [10]. The more negative potential and hydrogen site-blocking also results in a lower current efficiency to ECH for those catalysts (Fig. 4b). Although Pt<sub>86</sub>Co<sub>14</sub>/felt has the highest TOF of the catalysts for the conditions tested, it has a low current efficiency (Fig. 4b) due to high HER activity. The ECH TOF for Pt<sub>62</sub>Co<sub>38</sub>/felt instead increases with more negative potential along with a corresponding increase in current efficiency. This opposite behavior on Pt<sub>62</sub>Co<sub>38</sub>/felt may arise because the hvdrogen coverage is lower compared to Pt<sub>100</sub>/felt and Pt<sub>86</sub>Co<sub>14</sub>/felt, such that more negative potentials enhance ECH. The complicated trend in activity and current efficiency on the alloys suggests a more complicated model than a single adsorption energy descriptor is needed to understand phenol ECH on platinum cobalt alloys. To understand the multiple effects of adsorption energies and coverage, applied potential, and activation barriers, we use a kinetic model based on a Langmuir-Hinshelwood mechanism to capture the experimental trends. To construct this model, we first investigate the effects of Co fraction on phenol adsorption and the barrier for hydrogenation in the next section.

# 3.4. Effect of Co alloying on phenol adsorption and hydrogenation barriers

In aqueous phase, we do not find a significant change in the experimental adsorption free energy of phenol with increasing Co fraction (Fig. 5) despite the varying ECH TOF with Co fraction. We find the adsorption free energy of phenol to be  $-22.5 \, \text{kJ} \, \text{mol}^{-1}$ ,  $-19.0 \, \text{kJ} \, \text{mol}^{-1}$ , and  $-20.5 \, \text{kJ} \, \text{mol}^{-1}$  on Pt/C, Pt<sub>3</sub>Co/C, and PtCo/C, respectively. These adsorption energies were independent of phenol coverage. This constant aqueous phenol adsorption energy with Co fraction implies that the phenol adsorption energy is not an informative descriptor for ECH activity for these studied alloy systems. To extract the free energy for phenol adsorption, we fit the coverage vs. concentration data to a Temkin isotherm shown in Eq. (1).

$$\frac{\theta_{P}}{\theta_{sat}} = \frac{\exp\left(\frac{-(\Delta G_{ad_{d},\theta=0}^{aq} + a\theta_{P})}{RT}\right)C_{P}}{\left(1 + \exp\left(\frac{-(\Delta G_{ad_{d},\theta=0}^{aq} + a\theta_{P})}{RT}\right)C_{P}\right)}$$
(1)

Here  $\theta_P$  is the phenol coverage,  $\theta_{sat}$  is the saturation coverage,  $\Delta G_{ad\theta=0}^{aq}$  is the aqueous adsorption free energy in kJ mol<sup>-1</sup> at a phenol coverage of zero,  $\alpha$  is how adsorbate–adsorbate interactions influence the adsorption energy as a function of coverage in kJ mol<sup>-1</sup>, C<sub>P</sub> is the concentration of phenol, R is the ideal gas constant, and T is temperature in Kelvin. A caveat of these adsorption isotherms is that they probe the coverage of phenol as a function of bulk phenol concentration solely on the surface Pt atoms because the coverage of phenol on Co atoms cannot be probed using H<sub>UPD</sub>. We have previously shown that metals such as Pt and Rh which adsorb organic molecules (e.g., phenol) with very different energies in the gas phase have similar aqueous-phase adsorption energies [61]. We attributed this similar phenol adsorption between Pt and Rh to the energy penalty of displacing water molecules from the liquid/metal interface which offsets the energy difference observed in the gas phase (i.e., although Rh adsorbs phenol in the gas phase more strongly than Pt, it also adsorbs water more strongly, so the penalty for displacing water is larger on Rh than on Pt [72,73]).

Through DFT modeling, we demonstrate that the structure and composition of the alloy surface has a notable impact on the activation enthalpy of the first hydrogenation step. The DFT-predicted geometries for the first hydrogenation step of phenol on PtCo and Pt/PtCo are shown in Fig. 6a as representative examples. In Fig. 6b we show the computed activation enthalpy ( $\Delta H_f^{\dagger}$ ) as a function of Co fraction ( $y_{Co}$ ) for Pt<sub>x</sub>Co<sub>y</sub> and Pt/Pt<sub>x</sub>Co<sub>y</sub>. We calculate  $\Delta H_f^{\dagger}$  as the enthalpy of the transition state for the first hydrogenation step relative to the enthalpy of surface-adsorbed hydrogen and phenol. The activation enthalpy increases almost linearly with Co fraction on the Pt<sub>x</sub>Co<sub>y</sub> surfaces but decreases linearly with Co fraction for the Pt/Pt<sub>x</sub>Co<sub>y</sub> surfaces. The opposite trend in activation enthalpy with Co fraction on the two types of surfaces highlights the impact of having Co and Pt on the surface (Pt<sub>x</sub>Co<sub>y</sub>) compared to only Pt on the surface (Pt/Pt<sub>x</sub>Co<sub>y</sub>).

By comparing the activation enthalpy to the hydrogen adsorption enthalpy and hydrogenation reaction enthalpy, we observe why the  $Pt_xCo_y$  and  $Pt/Pt_xCo_y$  surfaces are predicted to have such different trends in hydrogenation rates with Co fraction. We show  $\Delta H_f^{\dagger}$  as a function of the computed hydrogen adsorption enthalpy ( $\Delta H_H$ ) on each respective surface in Fig. 6c. On the  $Pt/Pt_xCo_y$  surface,  $\Delta H_f^{\dagger}$  decreases with weakening hydrogen adsorption. We previously hypothesized that weakening hydrogen adsorption on a pure Pt catalyst through controlling the Pt

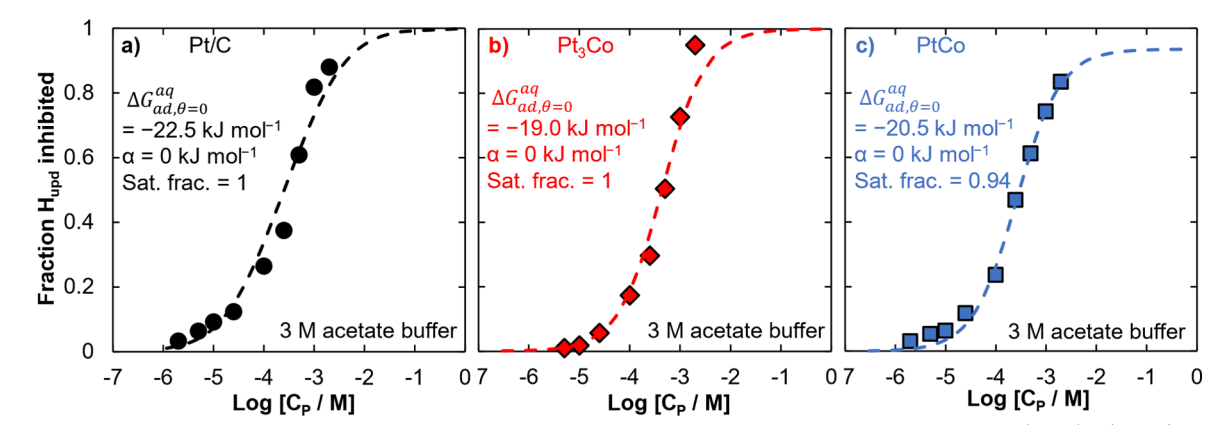


Fig. 5. Phenol adsorption energies from adsorption experiments on  $Pt_xCo_y/C$  catalysts. Phenol adsorption isotherm on a) Pt/C, b)  $Pt_3Co/C$ , and c) PtCo/C from inhibition of hydrogen underpotential deposition with different bulk phenol concentrations in 3 M acetate buffer and 23 °C. The dashed lines in a), b), and c) are fits of the data to a Temkin adsorption model to extract the aqueous adsorption energy and its coverage dependence  $\alpha$ .

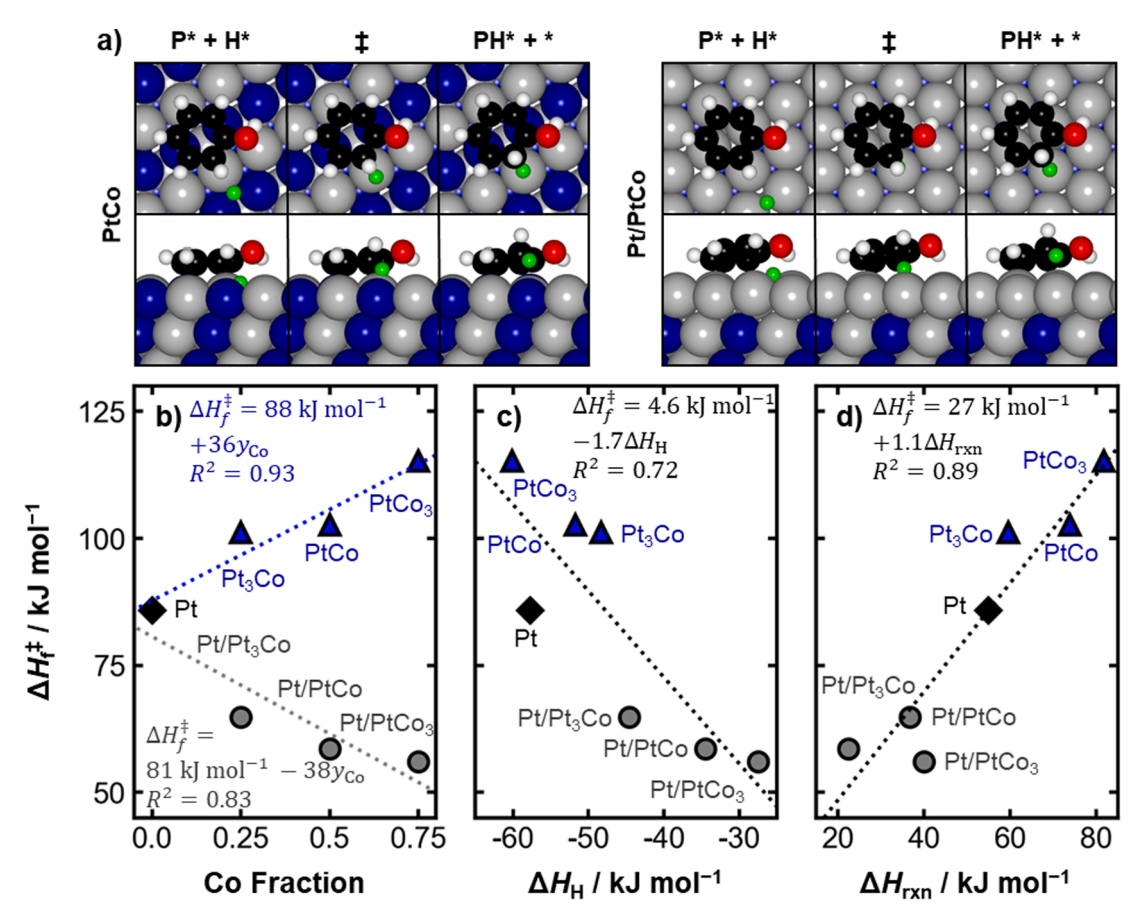


Fig. 6. Activation enthalpy for the first hydrogenation step of phenol. a) Top and side views of DFT-predicted geometries corresponding to the initial, transition, and final states for the first hydrogenation of phenol on the (111) facet of both PtCo and Pt/PtCo. Color legend: Pt = gray, Co = blue, O = red, C = black, and H = white. The H\* atom participating in the hydrogenation reaction is colored green. Activation enthalpy for the first hydrogenation of phenol on Pt<sub>x</sub>Co<sub>y</sub> and Pt/Pt<sub>x</sub>Co<sub>y</sub> as a function of b) Co fraction, c) the adsorption enthalpy of hydrogen ( $\Delta H_{\rm H}$ ), and d) the reaction enthalpy for the first hydrogenation step of phenol at 300 K ( $\Delta H_{\rm rxn}$ ). Blue triangles correspond to activation enthalpies calculated on Pt<sub>x</sub>Co<sub>y</sub> and gray circles correspond to barriers calculated on Pt/Pt<sub>x</sub>Co<sub>y</sub>. Black diamonds correspond to pure Pt. Linear fits to the data are shown along with corresponding equations. (For interpretation of the references to color in this figure legend, the reader is referred to the web version of this article.)

can influence the hydrogenation barrier through Brønsted-Evans-Polanyi (BEP) relations [74]. Briefly, with all else being held constant, a weaker adsorbed hydrogen would result in a more favorable hydrogenation reaction energy and consequently a lowered hydrogenation barrier. Although  $\Delta H_{\rm H}$  seems to be a descriptor for the Pt/Pt<sub>x</sub>Co<sub>v</sub> surfaces,  $\Delta H_f^{\dagger}$  is not simply a function of  $\Delta H_H$  for the  $\mathrm{Pt_xCo_v}$  surfaces. By examining  $\Delta H_f^{\dagger}$  on Pt<sub>x</sub>Co<sub>y</sub> as a function of the hydrogenation reaction enthalpy  $(\Delta H_{rxn})$  in Fig. 6d, we demonstrate that hydrogenation on Pt<sub>x</sub>Co<sub>v</sub> follows a BEP relationship, with a higher reaction enthalpy correlating with a higher activation enthalpy. The more endothermic ΔH<sub>rxn</sub> on the Pt<sub>x</sub>Co<sub>y</sub> surfaces compared Pt/Pt<sub>x</sub>Co<sub>y</sub> surfaces indicate that the hydrogenated intermediate species (PH\*) is less stable than the reactants (P\* + H\*) when there is Co in the surface catalyst layer. The slope near one implies a late transition state. For the Pt<sub>x</sub>Co<sub>y</sub> surfaces, the surface with the weakest hydrogen adsorption is not the surface with the least endothermic reaction enthalpy. Ultimately, despite adsorbed hydrogen being an important reactant, the hydrogen adsorption energy alone is not a suitable descriptor for phenol hydrogenation like it is for HER. Instead, the activation enthalpy more closely follows a BEP relationship, and the higher  $\Delta H_f^{\dagger}$  on  $Pt_xCo_y$  surfaces than on Pt or  $Pt/Pt_xCo_y$ surfaces is caused by the weaker interaction between the hydrogenated phenol intermediate and the PtxCoy surface.

# 3.5. Explaining ECH activity on $Pt_xCo_y$ alloys using a Langmuir-Hinshelwood model

We are able to describe the trend in experimental TOF with Co fractions and applied potentials shown in Fig. 4 using a Langmuir-Hinshelwood model to capture the effects of Co alloying on hydrogen adsorption energy, phenol adsorption energy, and hydrogenation activation enthalpy. Assuming that the first hydrogenation step is rate determining [9,10], we estimate the TOF as a function of potential and Co fraction using a simple microkinetic model. In Eq. (2), we show that the equilibrium adsorption coefficient for hydrogen ( $K_{\rm H}$ ) is a function of the applied electrochemical potential (E) and the hydrogen adsorption free energy on a given surface. F is Faraday's constant. We note that we assume the  $\Delta G_{\rm H}$  at 0 V vs. RHE here is the same as that computed for Fig. 1, referenced to 1 bar H<sub>2</sub>.

$$K_{\rm H}(E) = \exp\left(\frac{-\Delta G_{\rm H}(E=0~{
m V~vs.~RHE})}{RT}\right) \exp\left(\frac{-FE}{RT}\right)$$
 (2)

In Eq. (3), we assume that the phenol equilibrium adsorption coefficient  $(K_P)$  is independent of potential, although in reality there may be variations due to the impact of potential on the interfacial water layer [75]. The adsorption coefficient is dependent on the free energy of adsorption of phenol,  $\Delta G_{\text{ads.P}}$ .

$$K_{\rm P} = \exp\left(\frac{-\Delta G_{\rm ads,P}}{RT}\right) \tag{3}$$

If the first hydrogenation step is rate determining, the TOF will be described by Eq. (4). The TOF depends on the rate constant,  $k_{\rm ECH}$ , and the product of the hydrogen and phenol coverage,  $\theta_{\rm H}$  and  $\theta_{\rm P}$  [10]. The coverages are given by the equilibrium adsorption coefficients when adsorption is quasi-equilibrated. Here  $C_{\rm P}$  is the concentration of phenol and  $C_{\rm H}$  is an 'equivalent' chemical potential of hydrogen, as we have elaborated in previous work [61].

$$TOF = k_{ECH}\theta_{H}\theta_{P} = k_{ECH}\frac{K_{H}C_{H}K_{P}C_{P}}{\left(1 + K_{H}C_{H} + K_{P}C_{P}\right)^{2}}$$

$$\tag{4}$$

The rate constant depends on the enthalpy of the first hydrogenation step's transition state relative to the reactant energy ( $\Delta H_f^{\dagger}$ ) as we show in Eq. (5). A is a preexponential factor, which we assume to be independent of the Co content of the catalyst surface, and we do not include any influence of the applied potential on the rate constant.

$$k_{ECH} = A \exp\left(\frac{-\Delta H_{\rm f}^{\dagger}}{RT}\right) \tag{5}$$

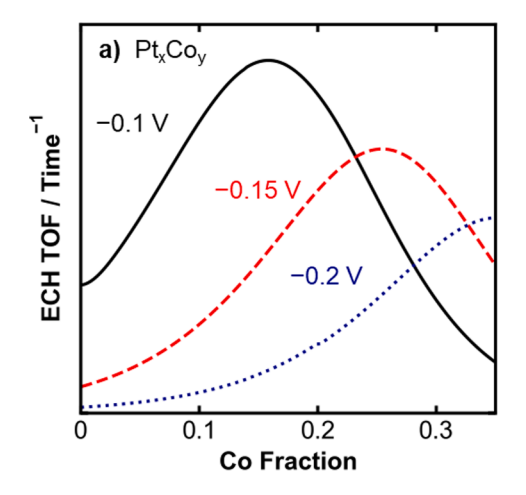
We predict the rate constant as a function of the Co fraction due to a dependence of the activation barrier on the Co fraction (Fig. 6b). The linear trends in Fig. 6b indicate that the rate constant would exponentially decrease with Co fraction on the mixed Co and Pt surface and exponentially increase with Co fraction on the Pt skin surface. As the hydrogen adsorption free energy is also a function of the Co fraction (Fig. 1b), we can describe the TOF as a function of Co content and potential if the first hydrogenation step is rate determining. Here we assume  $K_P$  is constant with Co content, and we use a  $\Delta G_{\text{ads},P}$  value of -9 kJ mol<sup>-1</sup> based on our previously obtained value for the adsorption energy of phenol on the active site of Pt for ECH [10]. Although, in principle, phenol adsorption strength is a descriptor for ECH activity based on the Langmuir-Hinshelwood mechanism, the measured phenol adsorption energy on Pt/C, Pt<sub>3</sub>Co/C, and PtCo/C was found to be nearly independent of the Co fraction and thus does not explain the variation in ECH activity of the alloys with respect to a change in the Co fraction. We discuss additional details of the kinetic model in the SI.

We show the prediction of the TOF as a function of potential and Co fraction in Fig. 7 for the two types of catalyst surfaces. The results on the mixed Co and Pt surface in Fig. 7a qualitatively match our experimental results in Fig. 4a. The relative hydrogen to phenol coverage decreases as Co fraction increases at a given potential (Figure S15a). The hydrogen coverage increases relative to phenol at a specified Co fraction as applied electrochemical potential becomes more negative, which is expected

from the potential dependence of hydrogen adsorption from protons in the CHE model. For higher Co fractions, where the hydrogen adsorption energy is weaker, the effect of more negative potential is less detrimental, as the phenol coverage remains high. In this way, the kinetic model captures why the maximum in ECH TOF with Co fraction varies as a function of applied potential. At comparable coverages of hydrogen and phenol for a pure Pt catalyst compared to a  $Pt_x Co_y$  alloy, the TOF is lower for the alloy due to the higher activation enthalpy (Fig. 6b). The increase in TOF with Co fraction observed experimentally at -0.1~V~vs. RHE in Fig. 4a is explained by our model as weakening the hydrogen adsorption energy, which allows a higher coverage of phenol on the surface, thus increasing the rate. Although this higher coverage of phenol results in an increase in the ECH rate, the current efficiency for ECH at -0.1~V~vs. RHE may be lower with Co fraction (Fig. 4b) because of an increase in the HER activity.

The data in **Figure S15b** shows the experimentally measured ECH TOF from Fig. 4 alongside the kinetic model predictions from Fig. 7a. For a given Co fraction, the trend in experimentally measured TOF matches that from the kinetic model. For example, at a Co fraction of zero, the order of the measured and predicted activities are -0.1 V > -0.15 V > -0.2 V, while at a Co fraction of 0.38, the order is -0.2 V > -0.15 V > -0.1 V. For a given potential, the trend in TOF with Co fraction is the same for experiment and the kinetic model at -0.1 V and -0.2 V. That is, at -0.1 V, the TOF increases with Co fraction at low Co content, then decreases. At -0.2 V the TOF in both experiment and the model increases with Co content for the entire Co fraction range studied. However, at -0.15 V the trend in Co fraction is not accurately captured.

The model for the TOF on a Pt skin with a  $Pt_xCo_y$  core (Fig. 7b) does not match our experimental values, further corroborating the mixed  $Pt_xCo_y$  surface indicated from our HER measurements, characterization, and DFT calculations of the energetically preferred surface. The decrease in activity at sufficiently high Co fractions is due to a decrease in the hydrogen coverage, conceptually similar to that described for Fig. 7a. In Fig. 7b, due to the prediction that an increasing Co fraction will decrease the hydrogenation barrier for a  $Pt/Pt_xCo_y$  structure, the ECH TOF is predicted to increase under almost all conditions up to high Co fractions, which is not what we observe experimentally. We predict a catalyst with a stable Pt skin and a  $Pt_xCo_y$  core structure under ECH conditions would be a more active catalyst based on DFT-calculated activation energies and our kinetic modeling. Further study of  $Pt/Pt_xCo_y$  core–shell alloys is needed to test the stability of  $Pt/Pt_xCo_y$  catalysts under ECH conditions and to experimentally verify the enhanced activity for phenol ECH.



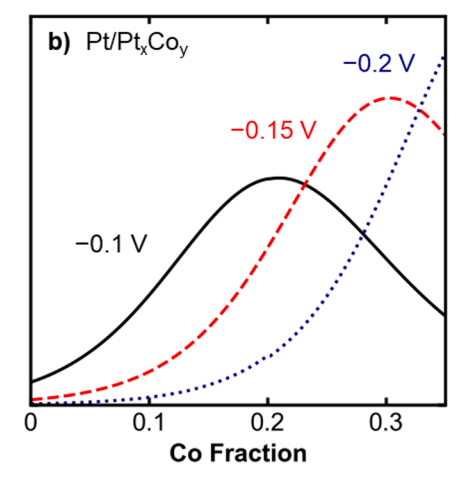


Fig. 7. ECH turnover frequency on  $Pt_xCo_y$  as a function of Co fraction and potential using a Langmuir-Hinshelwood model. a) Calculated ECH TOF assuming the first hydrogenation step is rate determining, and the transition state barrier increases as a function of Co fraction, as found for the for the mixed surface  $Pt_xCo_y$  structure ( $Pt_xCo_y$ ) in Fig. 6. b) Calculated ECH TOF assuming the first hydrogenation step is rate determining, and the transition state barrier is decreases as a function of Co fraction, as found for the Pt skin structure ( $Pt/Pt_xCo_y$ ) in Fig. 6. The temperature used is 300 K.

### 4. Conclusions

We find that Pt<sub>x</sub>Co<sub>y</sub> alloys at low Co fractions are more active toward ECH of phenol than pure Pt at -0.1 V vs. RHE, but the ECH current efficiency is lower than pure Pt due to their high HER activity. PtxCov preferentially forms structures with Co and Pt on the surface under our ECH and HER conditions, as opposed to a Pt skin. Although the HER activity correlates with computed hydrogen adsorption energies on Pt<sub>x</sub>Co<sub>v</sub> surfaces, with surfaces that adsorb hydrogen more weakly having higher HER activity, the hydrogen adsorption energy is an insufficient descriptor for ECH activity. Rather, the hydrogenation activation enthalpies follow a Brønsted-Evans-Polanyi relationship with respect to the reaction enthalpies, and the PtxCov surfaces have more endothermic reaction enthalpies and larger activation enthalpies than Pt despite adsorbing hydrogen more weakly. We qualitatively explain the experimental ECH TOF trends on the PtxCov surfaces with a Langmuir-Hinshelwood kinetic model. Our DFT and kinetic modeling predict that Pt/Pt<sub>x</sub>Co<sub>y</sub> alloys, i.e., a pure Pt surface layer with Pt<sub>x</sub>Co<sub>y</sub> core, would have enhanced ECH activity, although further work to synthesize and stabilize these structures under ECH conditions is needed.

### CRediT authorship contribution statement

James Akinola: Data curation, Formal analysis, Investigation, Methodology, Writing – original draft, Writing – review & editing. Isaiah Barth: Data curation, Formal analysis, Writing – original draft, Writing – review & editing. Bryan R. Goldsmith: Conceptualization, Formal analysis, Funding acquisition, Writing – original draft, Writing – review & editing, Supervision. Nirala Singh: Conceptualization, Formal analysis, Funding acquisition, Methodology, Project administration, Resources, Supervision, Writing – original draft, Writing – review & editing.

### **Declaration of Competing Interest**

The authors declare that they have no known competing financial interests or personal relationships that could have appeared to influence the work reported in this paper.

### Data availability

Data will be made available on request.

### Acknowledgments

This material is based upon work supported by the National Science Foundation under grant no. #1919444 and grant #2116646. Computing resources were provided by the Department of Energy, National Energy Research Scientific Computing Center (DE-AC02-05CH11231). This research used resources of the Advanced Photon Source Sector 20, a U.S. Department of Energy (DOE) Office of Science User Facility operated for the DOE Office of Science by Argonne National Laboratory under Contract No. DE-AC02-06CH11357, and the Canadian Light Source and its funding partners. The authors thank and acknowledge Chengjun Sun for help with X-ray absorption. The authors acknowledge the University of Michigan College of Engineering for financial support and the Michigan Center for Materials Characterization for use of the instruments and staff assistance.

### Appendix A. Supplementary material

Supplementary data to this article can be found online at https://doi.org/10.1016/j.jcat.2024.115331.

### References

- F.X. Aguilar, A. Saunders, Policy instruments promoting wood-to-energy uses in the continental United States, J. For. 108 (2010) 132–140.
- [2] E.J. Biddinger, O.Y. Gutierrez, J. Holladay, Electrochemical routes for biomass conversion, J. Appl. Electrochem. 51 (2021) 1–3, https://doi.org/10.1007/s10800-020-01525.x
- [3] M. Garedew, C.H. Lam, L. Petitjean, S. Huang, B. Song, F. Lin, J.E. Jackson, C. M. Saffron, P.T. Anastas, Electrochemical upgrading of depolymerized lignin: a review of model compound studies, Green Chem. 23 (2021) 2868–2899, https://doi.org/10.1039/D0GC04127K.
- [4] S.A. Akhade, N. Singh, O.Y. Gutiérrez, J. Lopez-Ruiz, H. Wang, J.D. Holladay, Y. Liu, A. Karkamkar, R.S. Weber, A.B. Padmaperuma, M.-S. Lee, G.A. Whyatt, M. Elliott, J.E. Holladay, J.L. Male, J.A. Lercher, R. Rousseau, V.-A. Glezakou, Electrocatalytic hydrogenation of biomass-derived organics: a review, Chem. Rev. 120 (2020) 11370–11419. https://doi.org/10.1021/acs.chemrev.0c00158.
- [5] A. Cyr, F. Chiltz, P. Jeanson, A. Martel, L. Brossard, J. Lessard, H. Ménard, Electrocatalytic hydrogenation of lignin models at Raney nickel and palladiumbased electrodes, Can. J. Chem. 78 (2000) 307–315, https://doi.org/10.1139/v00-009
- [6] Z. Li, M. Garedew, C.H. Lam, J.E. Jackson, D.J. Miller, C.M. Saffron, Mild electrocatalytic hydrogenation and hydrodeoxygenation of bio-oil derived phenolic compounds using ruthenium supported on activated carbon cloth, Green Chem. 14 (2012) 2540–2549, https://doi.org/10.1039/c2gc35552c.
- [7] C.H. Lam, C.B. Lowe, Z. Li, K.N. Longe, J.T. Rayburn, M.A. Caldwell, C.E. Houdek, J.B. Maguire, C.M. Saffron, D.J. Miller, J.E. Jackson, Electrocatalytic upgrading of model lignin monomers with earth abundant metal electrodes, Green Chem. 17 (2015) 601–609, https://doi.org/10.1039/C4GC01632G.
- [8] M. Kleinert, T. Barth, Phenols from lignin, Chem. Eng. Technol. 31 (2008) 736–745, https://doi.org/10.1002/ceat.200800073.
- [9] Y. Song, O.Y. Gutiérrez, J. Herranz, J.A. Lercher, Aqueous phase electrocatalysis and thermal catalysis for the hydrogenation of phenol at mild conditions, Appl. Catal. B Environ. 182 (2016) 236–246, https://doi.org/10.1016/j. apcatb.2015.09.027.
- [10] N. Singh, U. Sanyal, G. Ruehl, K.A. Stoerzinger, O.Y. Gutiérrez, D.M. Camaioni, J. L. Fulton, J.A. Lercher, C.T. Campbell, Aqueous phase catalytic and electrocatalytic hydrogenation of phenol and benzaldehyde over platinum group metals, J. Catal. 382 (2020) 372–384, https://doi.org/10.1016/j.jcat.2019.12.034.
- [11] S. Lu, C.A. Menning, Y. Zhu, J.G. Chen, Correlating benzene hydrogenation activity with binding energies of hydrogen and benzene on Co-based bimetallic catalysts, ChemPhysChem 10 (2009) 1763–1765, https://doi.org/10.1002/cphc.200.
- [12] P.T.M. Do, A.J. Foster, J. Chen, R.F. Lobo, Bimetallic effects in the hydrodeoxygenation of meta-cresol on γ-Al<sub>2</sub>O<sub>3</sub> supported Pt–Ni and Pt–Co catalysts, Green Chem. 14 (2012) 1388, https://doi.org/10.1039/c2gc16544a.
- [13] W.W. Lonergan, D.G. Vlachos, J.G. Chen, Correlating extent of Pt-Ni bond formation with low-temperature hydrogenation of benzene and 1,3-butadiene over supported Pt/Ni bimetallic catalysts, J. Catal. 271 (2010) 239–250, https://doi. org/10.1016/j.jcat.2010.01.019.
- [14] B.A. Cheney, J.A. Lauterbach, J.G. Chen, Reverse micelle synthesis and characterization of supported Pt/Ni bimetallic catalysts on  $\gamma$ -Al<sub>2</sub>O<sub>3</sub>, Appl. Catal. A Gen. 394 (2011) 41–47, https://doi.org/10.1016/j.apcata.2010.12.021.
- [15] K.A. Resende, C.E. Hori, F.B. Noronha, H. Shi, O.Y. Gutierrez, D.M. Camaioni, J. A. Lercher, Aqueous phase hydrogenation of phenol catalyzed by Pd and PdAg on ZrO<sub>2</sub>, Appl. Catal. A Gen. 548 (2017) 128–135, https://doi.org/10.1016/j.apcata.2017.08.005.
- [16] G.F. Santori, M.L. Casella, G.J. Siri, H.R. Adúriz, O.A. Ferretti, Effect of particle size in the hydrogenation of crotonaldehyde on supported Pt and Pt-Sn catalysts, React. Kinet. Mech. Catal. 75 (2002) 225–230, https://doi.org/10.1023/A: 1015234526107.
- [17] R.J. Meyer, Q. Zhang, A. Kryczka, C. Gomez, R. Todorovic, Perturbation of reactivity with geometry: how far can we go? ACS Catal. 8 (2018) 566–570, https://doi.org/10.1021/acscatal.7b03228.
- [18] W. Yu, M.D. Porosoff, J.G. Chen, Review of Pt-based bimetallic catalysis: from model surfaces to supported catalysts, Chem. Rev. 112 (2012) 5780–5817, https://doi.org/10.1021/cr300096b
- [19] M.P. Humbert, J.G. Chen, Correlating hydrogenation activity with binding energies of hydrogen and cyclohexene on M/Pt(111) (M = Fe Co, Ni, Cu) bimetallic surfaces, J. Catal. 257 (2008) 297–306, https://doi.org/10.1016/j. jcat.2008.05.013.
- [20] B. Liu, D. Xiao, Y. Wang, P. Jia, N. Huang, X. Lan, T. Wang, Correlating C=C, C=O, and C=N hydrogenation activity with hydrogen binding energies on Ni-Fe bimetallic catalysts, J. Phys. Chem. C 124 (2020) 18595–18603, https://doi.org/10.1021/acs.jpcc.0c04302.
- [21] J. Greeley, T.F. Jaramillo, J. Bonde, I. Chorkendorff, J.K. Nørskov, Computational high-throughput screening of electrocatalytic materials for hydrogen evolution, Nat. Mater. 5 (2006) 909–913, https://doi.org/10.1038/nmat1752.
- [22] J. Zheng, W. Sheng, Z. Zhuang, B. Xu, Y. Yan, Universal dependence of hydrogen oxidation and evolution reaction activity of platinum-group metals on pH and hydrogen binding energy, Sci. Adv. 2 (2016), https://doi.org/10.1126/ sciadv.1501602.
- [23] J.K. Nørskov, T. Bligaard, A. Logadottir, J.R. Kitchin, J.G. Chen, S. Pandelov, U. Stimming, Trends in the exchange current for hydrogen evolution, J. Electrochem. Soc. 152 (2005) J23, https://doi.org/10.1149/1.1856988.
- [24] S. Trasatti, Work function, electronegativity, and electrochemical behaviour of metals. III. Electrolytic hydrogen evolution in acid solutions, J. Electroanal. Chem. 39 (1972) 163–184, https://doi.org/10.1016/S0022-0728(72)80485-6.

- [25] O. Savadogo, D.L. Piron, New hydrogen cathodes in acid medium: Case of nickel electrodeposited with heteropolyacids (HPAs), Int. J. Hydrogen Energy 15 (1990) 715–721, https://doi.org/10.1016/0360-3199(90)90002-G.
- [26] E. Skúlason, V. Tripkovic, M.E. Björketun, S. Gudmundsdóttir, G. Karlberg, J. Rossmeisl, T. Bligaard, H. Jónsson, J.K. Nørskov, Modeling the electrochemical hydrogen oxidation and evolution reactions on the basis of density functional theory calculations, J. Phys. Chem. C 114 (2010) 18182–18197, https://doi.org/ 10.1021/jp1048887.
- [27] J. Greeley, J.K. Nørskov, Large-scale, density functional theory-based screening of alloys for hydrogen evolution, Surf. Sci. 601 (2007) 1590–1598, https://doi.org/ 10.1016/j.susc.2007.01.037.
- [28] P.N. Pintauro, M.P. Gil, K. Warner, G. List, W. Neff, Electrochemical hydrogenation of soybean oil with hydrogen gas, Ind. Eng. Chem. Res. 44 (2005) 6188–6195, https://doi.org/10.1021/ie0490738.
- [29] J. Ma, Z. Wang, T. Majima, G. Zhao, Role of Ni in PtNi alloy for modulating the proton–electron transfer of electrocatalytic hydrogenation revealed by the in situ Raman–rotating disk electrode method, ACS Catal. 12 (2022) 14062–14071, https://doi.org/10.1021/acscatal.2c03551.
- [30] Y. Du, X. Chen, C. Liang, Selective electrocatalytic hydrogenation of phenols over ternary Pt<sub>3</sub>RuSn alloy, Mol. Catal. 535 (2023) 112831, https://doi.org/10.1016/j. mcat.2022.112831.
- [31] M. Mavrikakis, B. Hammer, J.K. Nørskov, Effect of strain on the reactivity of metal surfaces, Phys. Rev. Lett. 81 (1998) 2819–2822, https://doi.org/10.1103/ PhysRevLett.81.2819.
- [32] X. Wang, Y. Zhu, A. Vasileff, Y. Jiao, S. Chen, L. Song, B. Zheng, Y. Zheng, S. Z. Qiao, Strain effect in bimetallic electrocatalysts in the hydrogen evolution reaction, ACS Energy Lett. 3 (2018) 1198–1204, https://doi.org/10.1021/acsenergylett.8b00454.
- [33] Y. Pan, D. Li, S. Sharma, C. Wang, M.J. Zachman, E.C. Wegener, A.J. Kropf, Y. S. Kim, D.J. Myers, A.A. Peterson, D.A. Cullen, J.S. Spendelow, Ordered CoPt oxygen reduction catalyst with high performance and durability, Chem. Catal. 2 (2022) 3559–3572, https://doi.org/10.1016/j.checat.2022.10.030.
- [34] J.R. Kitchin, J.K. Nørskov, M.A. Barteau, J.G. Chen, Role of strain and ligand effects in the modification of the electronic and chemical Properties of bimetallic surfaces, Phys. Rev. Lett. 93 (2004) 4–7, https://doi.org/10.1103/PhysRevLett.93.156801.
- [35] C. Wei, Y. Sun, G.G. Scherer, A.C. Fisher, M. Sherburne, J.W. Ager, Z.J. Xu, Surface composition dependent ligand effect in tuning the activity of nickel-copper bimetallic electrocatalysts toward hydrogen evolution in alkaline, J. Am. Chem. Soc. 142 (2020) 7765–7775, https://doi.org/10.1021/jacs.9b12005.
- [36] Y. Wang, L. Cao, N.J. Libretto, X. Li, C. Li, Y. Wan, C. He, J. Lee, J. Gregg, H. Zong, D. Su, J.T. Miller, T. Mueller, C. Wang, Ensemble effect in bimetallic electrocatalysts for CO<sub>2</sub> reduction, J. Am. Chem. Soc. 141 (2019) 16635–16642, https://doi.org/10.1021/jacs.9h05766.
- [37] W.M.H. Sachtler, R.A. Van Santen, Surface composition and selectivity of alloy catalysts, Adv. Catal. 26 (1977) 69–119, https://doi.org/10.1016/S0360-0564(08) 60070 V
- [38] N.V. Long, Y. Yang, C. Minh Thi, N. Van Minh, Y. Cao, M. Nogami, The development of mixture, alloy, and core-shell nanocatalysts with nanomaterial supports for energy conversion in low-temperature fuel cells, Nano Energy 2 (2013) 636–676, https://doi.org/10.1016/j.nanoen.2013.06.001.
- [39] M. Oezaslan, F. Hasché, P. Strasser, Pt-based core-shell catalyst architectures for oxygen fuel cell electrodes, J. Phys. Chem. Lett. 4 (2013) 3273–3291, https://doi. org/10.1021/jz4014135.
- [40] M. Oezaslan, F. Hasché, P. Strasser, Oxygen electroreduction on PtCo<sub>3</sub>, PtCo and Pt<sub>3</sub>Co alloy nanoparticles for alkaline and acidic PEM fuel cells, J. Electrochem. Soc. 159 (2012) B394–B405, https://doi.org/10.1149/2.075204jes.
- [41] M. Oezaslan, P. Strasser, Activity of dealloyed PtCo<sub>3</sub> and PtCu<sub>3</sub> nanoparticle electrocatalyst for oxygen reduction reaction in polymer electrolyte membrane fuel cell, J. Power Sources 196 (2011) 5240–5249, https://doi.org/10.1016/j. ipowsour\_2010.11.016.
- [42] M. Saquib, A. Halder, Dealloyed Pt<sub>3</sub>Co nanoparticles with higher geometric strain for superior hydrogen evolution reaction, J. Solid State Chem. 262 (2018) 229–236, https://doi.org/10.1016/j.jssc.2018.03.030.
- [43] I.N. Leontyev, D.Y. Chernyshov, V.E. Guterman, E.V. Pakhomova, A.V. Guterman, Particle size effect in carbon supported Pt-Co alloy electrocatalysts prepared by the borohydride method: XRD characterization, Appl. Catal. A Gen. 357 (2009) 1–4, https://doi.org/10.1016/j.apcata.2008.12.023.
- [44] N. Singh, M.T. Nguyen, D.C. Cantu, B.L. Mehdi, N.D. Browning, J.L. Fulton, J. Zheng, M. Balasubramanian, O.Y. Gutiérrez, V.A. Glezakou, R. Rousseau, N. Govind, D.M. Camaioni, C.T. Campbell, J.A. Lercher, Carbon-supported Pt during aqueous phenol hydrogenation with and without applied electrical potential: X-ray absorption and theoretical studies of structure and adsorbates, J. Catal. 368 (2018) 8–19, https://doi.org/10.1016/j.jcat.2018.09.021.
- [45] B. Ravel, M. Newville, ATHENA, ARTEMIS, HEPHAESTUS: data analysis for X-ray absorption spectroscopy using IFEFFIT, J. Synchrotron Radiat. 12 (2005) 537–541, https://doi.org/10.1107/S0909049505012719.
- [46] B.-W. Zhang, T. Sheng, Y.-X. Wang, X.-M. Qu, J.-M. Zhang, Z.-C. Zhang, H.-G. Liao, F.-C. Zhu, S.-X. Dou, Y.-X. Jiang, S.-G. Sun, Platinum-Cobalt bimetallic nanoparticles with Pt skin for electro-oxidation of ethanol, ACS Catal. 7 (2017) 892–895, https://doi.org/10.1021/acscatal.6b03021.
- [47] P.J. Dietrich, M.C. Akatay, F.G. Sollberger, E.A. Stach, J.T. Miller, W.N. Delgass, F. H. Ribeiro, Effect of Co loading on the activity and selectivity of PtCo aqueous phase reforming catalysts, ACS Catal. 4 (2014) 480–491, https://doi.org/10.1021/cs4008705.

- [48] G. Kresse, J. Furthmüller, Efficiency of ab-initio total energy calculations for metals and semiconductors using a plane-wave basis set, Comput. Mater. Sci. 6 (1996) 15–50, https://doi.org/10.1016/0927-0256(96)00008-0.
- [49] G. Kresse, J. Furthmüller, Efficient iterative schemes for ab initio total-energy calculations using a plane-wave basis set, Phys. Rev. B 54 (1996) 11169–11186, https://doi.org/10.1103/PhysRevB.54.11169.
- [50] G. Kresse, J. Hafner, Ab initio molecular dynamcis for liquid metals, Phys. Rev. B 47 (1993) 558, https://doi.org/10.1103/PhysRevB.47.558.
- [51] G. Kresse, J. Hafner, Ab initio molecular-dynamics simulation of the liquid-metalamorphous- semiconductor transition in germanium, Phys. Rev. B 49 (1994) 14251–14269, https://doi.org/10.1103/PhysRevB.49.14251.
- [52] J.P. Perdew, K. Burke, M. Ernzerhof, Generalized gradient approximation made simple, Phys. Rev. Lett. 77 (1996) 3865–3868, https://doi.org/10.1103/ PhysRevLett.77.3865.
- [53] S. Grimme, J. Antony, S. Ehrlich, H. Krieg, A consistent and accurate ab initio parametrization of density functional dispersion correction (DFT-D) for the 94 elements H-Pu, J. Chem. Phys. 132 (2010) 154104, https://doi.org/10.1063/ 1.3382344.
- [54] P.E. Blöchl, Projector augmented-wave method, Phys. Rev. B 50 (1994) 17953–17979, https://doi.org/10.1103/PhysRevB.50.17953.
- [55] G. Kresse, D. Joubert, From ultrasoft pseudopotentials to the projector augmentedwave method, Phys. Rev. B 59 (1999) 1758–1775, https://doi.org/10.1103/ PhysRevB.59.1758.
- [56] M. Methfessel, A.T. Paxton, High-precision sampling for Brillouin-zone integration in metals, Phys. Rev. B 40 (1989) 3616–3621, https://doi.org/10.1103/ PhysRevB 40 3616
- [57] H.J. Monkhorst, J.D. Pack, Special points for Brillouin-zone integrations, Phys. Rev. B 13 (1976) 5188–5192, https://doi.org/10.1103/PhysRevB.13.5188.
- [58] I. Barth, J. Akinola, J. Lee, O.Y. Gutiérrez, U. Sanyal, N. Singh, B.R. Goldsmith, Explaining the structure sensitivity of Pt and Rh for aqueous-phase hydrogenation of phenol, J. Chem. Phys. 156 (2022) 104703, https://doi.org/10.1063/ 5.008208
- [59] U. Sanyal, Y. Song, N. Singh, J.L. Fulton, J. Herranz, A. Jentys, O.Y. Gutiérrez, J. A. Lercher, Structure sensitivity in hydrogenation reactions on Pt/C in aqueous-phase, ChemCatChem 11 (2019) 575–582, https://doi.org/10.1002/cctc.201801344.
- [60] G. Henkelman, B.P. Uberuaga, H. Jónsson, A climbing image nudged elastic band method for finding saddle points and minimum energy paths, J. Chem. Phys. 113 (2000) 9901–9904, https://doi.org/10.1063/1.1329672.
- [61] J. Akinola, I. Barth, B.R. Goldsmith, N. Singh, Adsorption energies of oxygenated aromatics and organics on rhodium and platinum in aqueous phase, ACS Catal. 10 (2020) 4929–4941, https://doi.org/10.1021/acscatal.0c00803.
- [62] S. Kobayashi, D.A. Tryk, H. Uchida, Enhancement of hydrogen evolution activity on Pt-skin/Pt3Co [(111), (100), and (110)] single crystal electrodes, Electrochem. Commun. 110 (2020) 106615, https://doi.org/10.1016/j.elecom.2019.106615.
- Commun. 110 (2020) 106615, https://doi.org/10.1016/j.elecom.2019.106615.
  [63] F. Guo, Z. Zou, Z. Zhang, T. Zeng, Y. Tan, R. Chen, W. Wu, N. Cheng, X. Sun, Confined sub-nanometer PtCo clusters as a highly efficient and robust electrocatalyst for the hydrogen evolution reaction, J. Mater. Chem. A 9 (2021) 5468–5474, https://doi.org/10.1039/d0ta10500g.
- [64] T. Anniyev, S. Kaya, S. Rajasekaran, H. Ogasawara, D. Nordlund, A. Nilsson, Tuning the metal-adsorbate chemical bond through the ligand effect on platinum subsurface alloys, Angew. Chem. Int. Ed. 51 (2012) 7724–7728, https://doi.org/ 10.1002/anje.201201068
- [65] X. Zhang, H. Wang, J. Key, V. Linkov, S. Ji, X. Wang, Z. Lei, R. Wang, Strain effect of core-shell Co@Pt/C nanoparticle catalyst with enhanced electrocatalytic activity for methanol oxidation, J. Electrochem. Soc. 159 (2012) B270–B276, https://doi. org/10.1149/2.015203jes.
- [66] M.P. Hyman, J.W. Medlin, Effects of electronic structure modifications on the adsorption of oxygen reduction reaction intermediates on model Pt(111)-alloy surfaces, J. Phys. Chem. C 111 (2007) 17052–17060, https://doi.org/10.1021/ jp075108g.
- [67] I.T. McCrum, M.T.M. Koper, The role of adsorbed hydroxide in hydrogen evolution reaction kinetics on modified platinum, Nat. Energy 5 (2020) 891–899, https:// doi.org/10.1038/s41560-020-00710-8.
- [68] Y. Qiu, L. Xin, Y. Li, I.T. McCrum, F. Guo, T. Ma, Y. Ren, Q. Liu, L. Zhou, S. Gu, M. J. Janik, W. Li, BCC-phased PdCu alloy as a highly active electrocatalyst for hydrogen oxidation in alkaline electrolytes, J. Am. Chem. Soc. 140 (2018) 16580–16588, https://doi.org/10.1021/jacs.8b08356.
- [69] H. Luo, V.Y. Yukuhiro, P.S. Fernández, J. Feng, P. Thompson, R.R. Rao, R. Cai, S. Favero, S.J. Haigh, J.R. Durrant, I.E.L. Stephens, M.M. Titirici, Role of Ni in PtNi bimetallic electrocatalysts for hydrogen and value-added chemicals coproduction via glycerol electrooxidation, ACS Catal. 12 (2022) 14492–14506, https://doi.org/ 10.1001/(preparal/2013007)
- [70] Q. Jia, Z. Zhao, L. Cao, J. Li, S. Ghoshal, V. Davies, E. Stavitski, K. Attenkofer, Z. Liu, M. Li, X. Duan, S. Mukerjee, T. Mueller, Y. Huang, Roles of Mo surface dopants in enhancing the ORR performance of octahedral PtNi nanoparticles, Nano Lett. 18 (2018) 798–804, https://doi.org/10.1021/acs.nanolett.7b04007.
- [71] R. Subbaraman, D. Tripkovic, K.-C. Chang, D. Strmcnik, A.P. Paulikas, P. Hirunsit, M. Chan, J. Greeley, V. Stamenkovic, N.M. Markovic, Trends in activity for the water electrolyser reactions on 3d M(Ni Co, Fe, Mn) hydr(oxy)oxide catalysts, Nat. Mater. 11 (2012) 550–557, https://doi.org/10.1038/nmat3313.
- [72] N. Singh, C.T. Campbell, A simple bond-additivity model explains large decreases in heats of adsorption in solvents versus gas phase: a case study with phenol on Pt (111) in water, ACS Catal. 9 (2019) 8116–8127, https://doi.org/10.1021/ acscatal.9b01870.

- [73] J. Akinola, C.T. Campbell, N. Singh, Effects of solvents on adsorption energies: A [73] J. Akhilota, C.T. Campbell, N. Singli, Effects of Solvents on adsorption energies. A general bond-additivity model, J. Phys. Chem. C 125 (2021) 24371–24380, https://doi.org/10.1021/acs.jpcc.1c06781.
  [74] N. Singh, M. Lee, S.A. Akhade, G. Cheng, D.M. Camaioni, O.Y. Gutiérrez, V. Glezakou, R. Rousseau, J.A. Lercher, C.T. Campbell, Impact of pH on aqueous-
- phase phenol hydrogenation catalyzed by carbon-supported Pt and Rh, ACS Catal. 9 (2019) 1120–1128, https://doi.org/10.1021/acscatal.8b04039.
- [75] J.O. Bockris, K.T. Jeng, In-situ studies of adsorption of organic compounds on platinum electrodes, J. Electroanal. Chem. 330 (1992) 541–581, https://doi.org/ 10.1016/0022-0728(92)80330-7.